Geophys. J. Int. (1990) **100,** 131–151

Upper mantle structure under western Europe from fundamental and higher mode surface waves using the NARS array

Bernard Dost*

Department of Theoretical Geophysics, Institute of Earth Sciences, PO Box 80.021, 3508 *TA Utrecht, The Netherlands*

Accepted 1989 August 11. Received 1989 August 11; in original form 1988 December 14

SUMMARY

A generalized inversion of a new data set, consisting of surface wave phase velocities and S_n traveltimes, has resulted in a new shear velocity and density model for the west-European platform (WEPL2). The surface wave phase velocity data set consists of fundamental and higher mode (mode 1–6) measurements from 25 to 70 mHz, using the Network of Autonomously Recording Stations (NARS) array, which was specifically designed for higher mode surface wave measurements. The S_n traveltime data set consists of ISC readings for selected European events. Major features of WEPL2 are a high-velocity lid of 80–140 km depth, underlain by a pronounced low-velocity zone between 160 and 220 km depth. The transition zone (400–650 km depth) is characterized by high shear velocities with respect to PREM. The density shows a positive gradient from 60 to 140 km depth, followed by an approximately constant value down to 400 km depth. A model for the Baltic shield (SCSH2) is obtained by combination of Nolet's (1977) higher mode phase velocity data set for western Europe including the Baltic shield and the present phase velocities for the platform. This shield model shows an absence of the low-velocity layer and low shear velocities in the top of the transition layer with respect to WEPL2. Density, although less well resolved, shows lower values for the shield structure between 200 and 350 km depth.

Key words: Europe, NARS, upper mantle, surface waves.

INTRODUCTION

The primary objective of the digital, broad-band NARS array, operational as a linear array from 1983 to 1987, is to measure the dispersion of higher mode surface waves for the west-European platform (Nolet & Vlaar 1982; Nolet, Dost & Paulssen 1986a). Inversion of these dispersion measurements for shear velocity and density provides us with a regional upper-mantle model. The use of higher mode surface waves guarantees that such a model has good resolution, capable of resolving horizontal layering within 50 km depth intervals or better. Although only simple vertically stratified (laterally homogeneous) models result from this analysis, such regional models can test current hypotheses about the structure and composition of the upper mantle.

Measurement of the dispersion of higher mode surface waves is complicated by the fact that these waves show up in the seismogram as an interfering mode group. Stacking methods (Nolet 1975, 1977; Nolet & Panza 1976; Cara 1978), applied to seismometer arrays with apertures in excess of 1000 km, make higher mode dispersion analysis possible. In this way accurate models of the average upper mantle structure under the array (independent of the rest of the wave path) have been obtained. More recently, methods have been developed to directly invert waveforms (Lerner-Lam & Jordan 1983; Nolet, van Trier & Huisman 1986). Although these methods do not require an array of stations, they require the existence of a good starting model and provide information on the averaged structure over the full length of the wave path between source and receiver.

In this study we present results of the application of the stacking technique to data from the NARS array. Preliminary measurements (Dost 1986) indicated that, by using NARS, higher mode Rayleigh wave phase velocities can be obtained for frequencies up to 70 mHz. In comparison to earlier measurements in Europe, including the Baltic shield (Nolet 1977; Cara, Nercessian & Nolet 1980), this is an extension of 30 mHz towards the high frequencies. Inversion of the data set for isotropic shear wave velocity and density yielded a smooth shear wave velocity model without a clear Lehmann discontinuity,

* Now at the ORFEUS Data Center, Inst. of Earth Sciences, PO Box 80.021, 3508 TA Utrecht, The Netherlands.

but with a possible steep positive density gradient from 60 to 100 km depth. A comparison with previous measurements for western Europe including the Baltic shield (Nolet 1977) showed differences between shield and platform structure; the shield structure is characterized by higher shear wave velocities down to 300 km depth.

Encouraged by these preliminary results we tried to refine them. Refinements presented here consist of the development of resolution enhancement techniques for the higher mode dispersion measurements, extension of the Rayleigh wave phase velocity measurements to lower frequencies and inclusion of Love wave data and S_n traveltimes in the inversion to constrain the shear-wave velocity in the uppermost mantle. In presenting the inversion of this data set we discuss the class of models that fit the data and present our preferred model for the west-European platform. In addition we discuss a refined shield model.

An interpretation of the preliminary results in terms of mantle mineralogy (Nolet *et al.* 1986b) strongly suggested the existence of a layer of eclogitic composition between 80 and 120 km depth. Since this publication, a wealth of new laboratory measurements has become available, aiding in the interpretation of seismological models in terms of mantle stucture and mineralogy. We thus interpret our models in the framework of this discussion.

DATA

For optimal analysis of higher modes, earthquakes must be located near the great circle through the NARS stations. In the period 1983–1987 three Japanese events and one Kurile event (Table 1, Fig. 1) were recorded at a sufficient number of NARS stations (seven or more) to carry out a higher mode analysis. One additional Japanese event (1983 May 26) that was recorded with good quality records at only six stations has also been used. This event was included since its location coincides with the events of 1983 June 21 and their moment tensor solutions are very similar; an attempt was made to process these two events together in one stack. Surprisingly, one event in NW Africa occurred on the great circle at the end of 1983 and was recorded at seven stations. Higher mode surface wave excitation is most effective for a source at intermediate depth ($100 < z < 300$ km). Unfortunately no such event with sufficient magnitude occurred during this investigation.

Table 1. List of events used in this analysis. The last column gives the number of stations that recorded the event.

date	origin time	lon	lat	depth	mb	Region	# stat.
26/05/83	2:59:58.8	139.09E	40.48N	16	6.6	Honshu	6
21/06/83	6:25:26.8	139.10E	41.35N	6	6.5	Honshu	8
22/12/83	4:11:29.3	13.51W	11.85N	11	6.3	NW Africa	7
06/03/84	2:17:21.0	138.92E	29.35N	454	6.1	E. Honshu	9
24/03/84	9:44:02.3	148.12E	44.04N	42	6.1	Kuriles	10
18/09/84	17:02:40.7	141.64E	34.01N	20	6.5	Honshu	9

The NW Africa (1983 December 22) and Kurile (1984 March 24) events are situated precisely on the great circle through the NARS array. The Japanese events are close to the great circle; the maximum deviation in azimuth is a maximum of 12° for the 1984 March 6 event. Since this is considerably less than the maximum deviation in azimuth in previous studies, which gave good results, we assume that we can neglect the variation of the initial phase. This simplifies the application of the stacking technique. Vertical component recordings (e.g. Fig. 2), provided the Rayleigh wave data. The horizontal components, although less stable, were used for Love wave data. The data were checked for possible timing errors and polarity reversals by comparison of P and S onsets and surface wave polarities along the array. In cases where timing could not be checked, due to the temporary absence of an accurate timing signal, the onset times of P and S arrivals were calculated using PEM-C model and compared with the data. Epicentre determinations were taken from the ISC bulletin.

The vertical and radial component of the shallow Japanese/Kurile events show a pulse-like arrival with a group velocity of approximately 5.2 km s^{-1} and dominant period of 40 s between the predicted *SS* and *SSS* arrivals (Fig. 3). The transverse component shows a similar phase at a group velocity of 4.5 km s^{-1}. Nakada & Hashizume (1983), in a study of the upper mantle beneath the Canadian shield, used similar pulse-like signals as higher mode surface wave data and identified the signal on the transverse component as a S_a phase. A similar phase on the vertical and radial component with group velocity between 4.6 and 4.8, called the Rayleigh type S_a phase, has not been found in our data set.

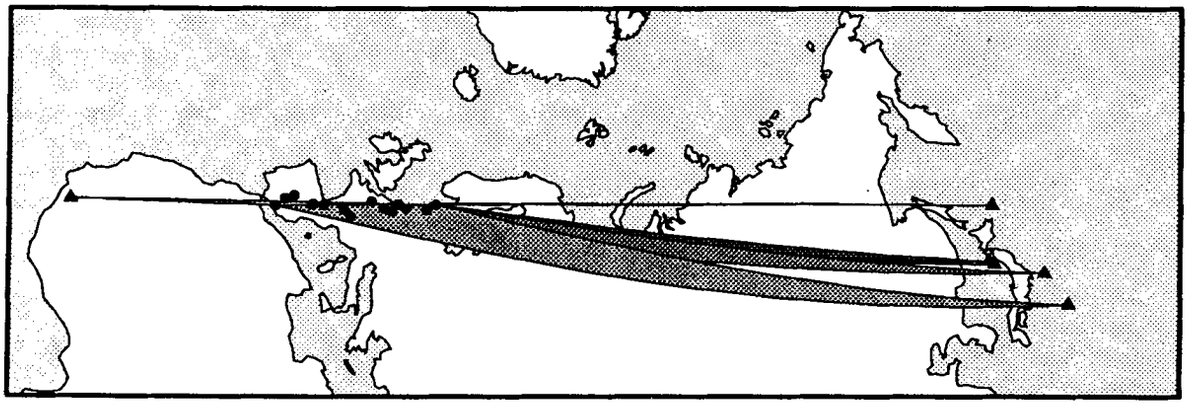

Figure 1. Locations of the earthquakes used in the analysis.

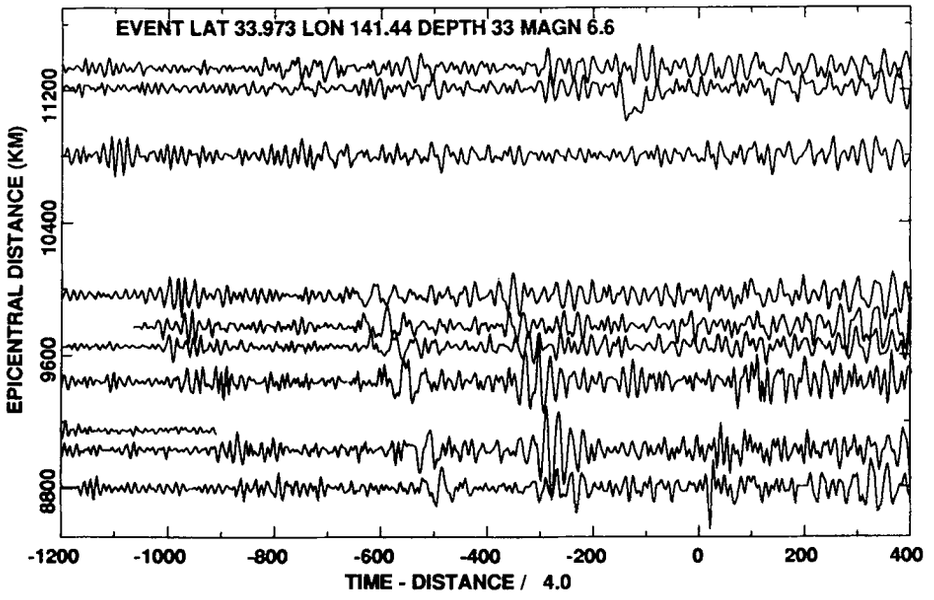

Figure 2. Vertical component NARS recording of the 1984 September 18 Honshu event.

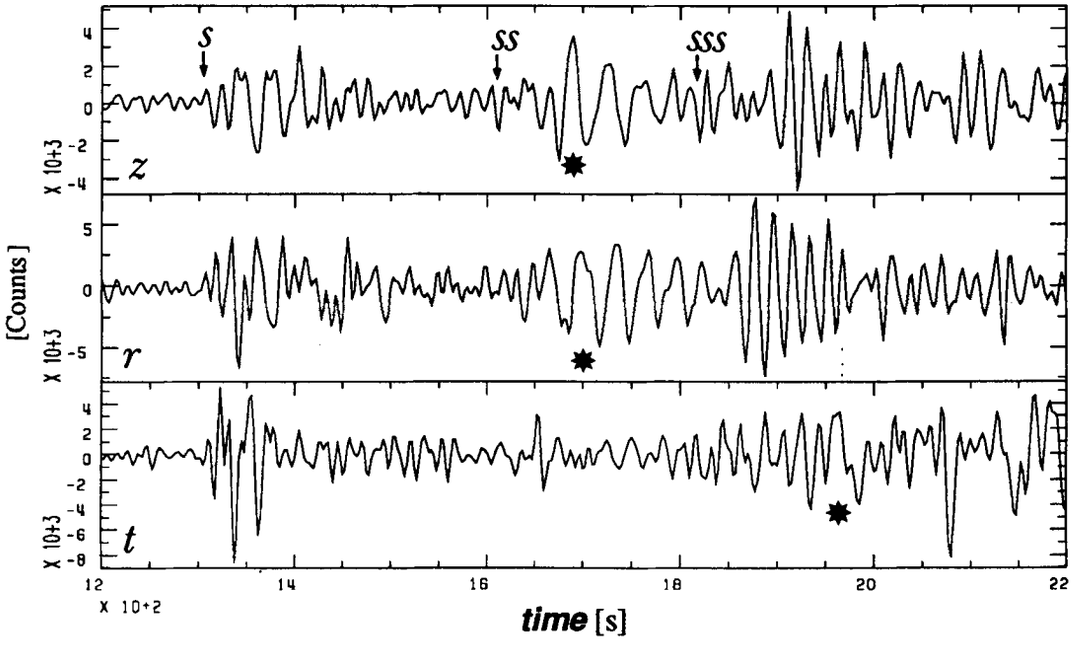

Figure 3. Vertical, radial and transverse component of the 1984 March 24 event recorded in NARS station NE04. Pulse-like arrivals are marked with a star.

STACKING TECHNIQUE

Higher mode surface waves show up in the seismogram as a pattern of interfering waves arriving in the time interval between the *S*-onset and the fundamental mode surface wave. In order to separate the different modes we transform the frequency spectrum $w(\Delta, \omega)$ of the signal $s(\Delta, t)$ to the complex wavenumber spectrum $W(k, \omega)$:

$$W(k, \omega) = \int_{-\infty}^{\infty} w(\Delta, \omega) e^{-ik\Delta}\, d\Delta \qquad (1)$$

where k denotes the wavenumber, ω angular frequency and Δ epicentral distance. By showing the equivalence between surface waves and normal modes in the limit for large radial orders, Nolet (1976) derived an expression for the frequency spectrum:

$$w(\Delta_j, \omega) = \sum_{n=1}^{M} F_{nj}(\omega) e^{ik_n(\omega)\Delta_j + i\phi_{nj}(\omega)} \qquad (2)$$

where $F_{nj}(\omega)$ is the amplitude of mode n at station j, $k_n(\omega)$ is the wavenumber of mode n and ϕ_{nj} is the initial phase

which depends on the azimuth from the source. The most important approximation made in the derivation of equation (2), use of the asymptotic representation of a Legendre polynomial for $\Delta \gg 0$, imposes limits on the location of the array with respect to the source. Panza, Schwab & Knopoff (1973) determined a condition for three-figure accuracy in amplitude and phase: $k\Delta > 10$, which is appropriate for the measurements presented here. If stations do not differ considerably in azimuth and if the array is not situated near a minimum of the radiation pattern we can neglect the variations of $\phi_{nj}(\omega)$ in the different stations (Nolet & Panza 1976). The amplitude F_{nj} is a function of station position, but the effect of dissipation over the array is small. We will therefore neglect the station dependence in the amplitude. If necessary, we can correct for the geometrical spreading. Combination of equation (1) and (2) without station dependence of amplitude and initial phase gives,

$$W(k, \omega) = 2\pi \sum_{n=1}^{M} F_n(\omega) e^{i\phi_n(\omega)} \delta(k_n - k). \tag{3}$$

The complex wavenumber spectrum consists of a set of M delta functions $\delta(k_n - k)$, centred around the modes n. Unfortunately, we have a finite number of recording stations and therefore we can only make an estimate $\bar{W}(k)$ of $W(k)$;

$$\bar{W}(k, \omega) = \frac{1}{N} \sum_{j=1}^{N} a(\Delta_j, \omega) w(\Delta_j, \omega) e^{-ik\Delta_j}. \tag{4}$$

The contribution of each station j is weighted by a factor $a(\Delta_j, \omega)$. These weighting factors are assumed to be equal to unity in the above presented theory, but can be chosen $\neq 1$ in order to enhance the signal-to-noise ratio in the frequency–wavenumber domain. Combination of equation (4) and (2) gives at constant frequency:

$$\bar{W}(k) = \sum_{n=1}^{M} F_n e^{i\phi_n} \mathrm{H}(k_n - k),$$
$$\mathrm{H}(k) = \frac{1}{N} \sum_{j=1}^{N} a(\Delta_j) e^{ik\Delta_j}. \tag{5}$$

$|\mathrm{H}(k)|^2$ is called the array response function and its shape determines the resolution of the measurements. $|\mathrm{H}(k)|$, a delta function in the limit of many stations, is only approximately so for a limited number. Here $|\mathrm{H}(k)|$ is peaked about $k = 0$, but has many secondary minima, essentially due to spatial aliasing.

Accurate determination of the phase velocity of mode n can be obtained if the number of modes present in the signal is small. Therefore segments of the seismic signal are windowed in the time domain around a traveltime $\tau = \Delta_j / v_g$ and the estimator (4) is calculated at a selected frequency (ω_0). This procedure is repeated for a suite of group velocities and results in a mode separation diagram, where $|\bar{W}(k, \omega)|^2$ is plotted as a function of phase and group velocity at frequency ω_0 (Fig. 4a). Phase velocity (c) and wavenumber (k) are related through $c = \omega/k$. Modes show up as maxima in the mode-separation diagram. Since we know the locations of the stations, and thus the shape of the array response function, we can correct the wavenumber spectrum for the effect of spatial aliasing and possible non-equidistant sampling. The CLEAN algorithm, introduced in seismology by Nolet & Panza (1976), iteratively carries out this procedure. However, the use of this algorithm is restricted to cases where only a few modes are present, in our case the low-frequency part of the spectrum.

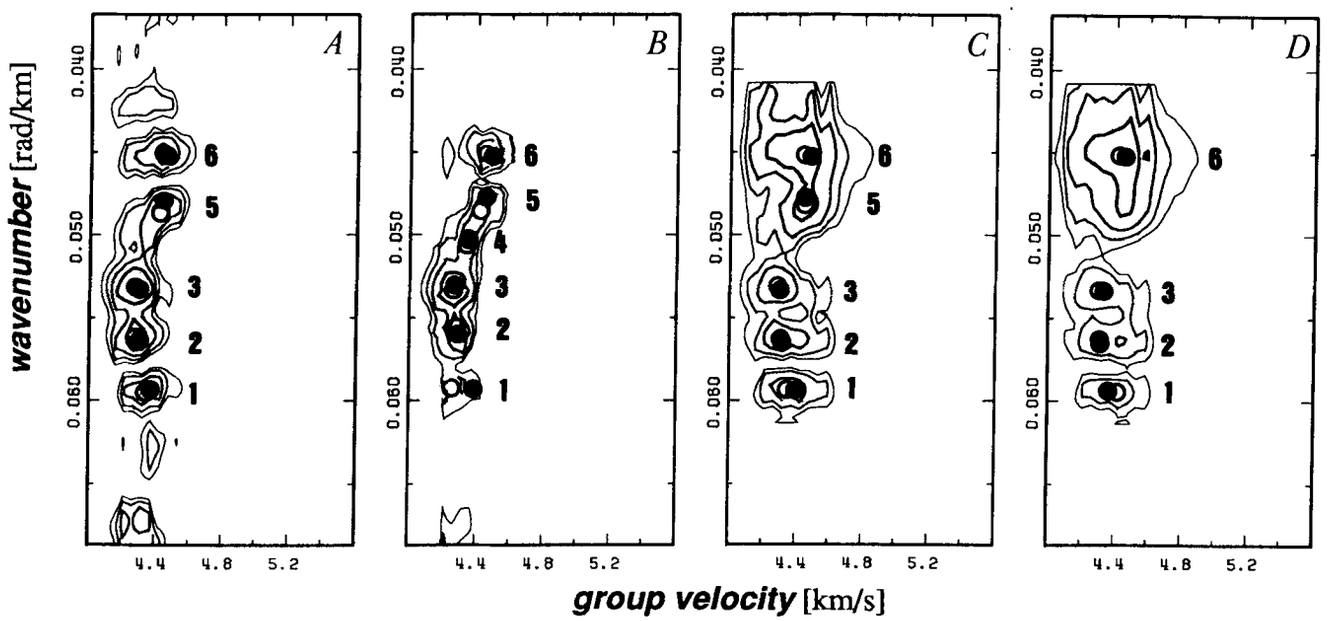

Figure 4. Mode separation diagrams at a period of 22.85 s for: A, DFT stack; B, DFT + CLEAN; C, PDFT stack with $\varepsilon = 0.1$ per cent; and D, PDFT stack with $\varepsilon = 0.01$ per cent. ε is given in percentage relative to the height of the 'boxes'. The diagram is scaled on its maximum and contours are given in dB from this maximum, and individual modes are numbered. The contour interval is 2.5 dB. Diagrams are for the analysis of a synthetic section. Closed circles give theoretical, open circles give calculated mode dispersion values.

A performance test on a synthetic data set (Dost 1987) showed that CLEAN introduces a bias in the measurements for frequencies higher than 35 mHz, which is within our frequency range of interest. This is illustrated in Fig. 4(b), where the measured phase and group velocities for mode 1, 5 and 6 do not coincide with the theoretical ones although mode 4 is resolved, in contrast with Fig. 4(a).

Cara (1978) shows that it is useful to choose weights $a(\Delta_j)$ in order to manipulate the array response function. To achieve this he designed a penalty function that was subsequently minimized. A more general theory for determination of optimal weighting is given by Dost (1987), who showed how to evaluate the effectiveness of weighting for an arbitrary station configuration. However, due to the limited number of stations that recorded the events processed, weighted stacking did not produce improvements in the accuracy of the measurements. We therefore investigated whether the above described stacking technique can be improved by modifying the estimator equation (4).

FOURIER ESTIMATORS INCORPORATING *A PRIORI* KNOWLEDGE

We can incorporate *a priori* knowledge about the spectrum in the Fourier estimator itself. This theory has been developed in a different framework by Byrne & Fitzgerald (1982, 1984) and Michette *et al.* (1984). Since we know the approximate location in the frequency–wavenumber domain of the modes from previous studies, these techniques should improve the accuracy of the measurements.

We incorporate our *a priori* knowledge about the shape of the wavenumber spectrum $W(k)$ in a function $P(k)$:

$$P(k) = A_n + \varepsilon, \quad k_n - \kappa_n \le k \le k_n + \kappa_n, \quad n = 0, 1, 2, \ldots,$$
$$= \varepsilon, \quad \text{otherwise}, \tag{6}$$

with k_n the *a priori* known wavenumber of mode n, κ_n the uncertainty in the *a priori* knowledge, A_n the amplitude of mode n in the stack and ε a damping parameter. $P(k)$ is thus defined as a series of 'boxes', centred at modes n. If we assume $W(k)$ to be a member of the weighted Hilbert space $H = L^2\left(-\infty, \infty; \frac{1}{P(k)}\right)$ with inner product

$$\langle Y(k), Z(k)\rangle_p = \int_{-\infty}^{\infty} Y(k)Z^*(k)\,\frac{1}{P(k)}\,\frac{dk}{2\pi}, \tag{7}$$

we can write:

$$w(\Delta_j) = \int_{-\infty}^{\infty} W(k)e^{ik\Delta_j}\frac{dk}{2\pi} = \langle W(k), g_j(k)\rangle_p,$$
$$g_j(k) = e^{ik\Delta_j}P(k). \tag{8}$$

An estimator $\bar{W}(k)$ can now be constructed, as in Backus–Gilbert theory, using the data kernels g_j as a set of basis functions:

$$\bar{W}(k) = \sum_{j=1}^{N} b_j g_j(k). \tag{9}$$

In contrast to the estimator (4), based on a discrete Fourier transform (DFT), our parameters b_j are not equivalent to the (un)weighted spectral values $w(\Delta_j)$. To construct our estimator from the data $w(\Delta_j)$, we minimize the weighted norm;

$$\int_{-\infty}^{\infty}\left|W(k) - \sum_{j=1}^{N} b_j P(k)e^{-ik\Delta_j}\right|^2 \frac{1}{P(k)}\,dk. \tag{10}$$

Differentiation with respect to b_n yields

$$\int_{-\infty}^{\infty} W(k)e^{ik\Delta_n}\frac{dk}{2\pi} = \sum_{j=1}^{N} b_j\int_{-\infty}^{\infty} P(k)e^{ik(\Delta_n-\Delta_j)}\frac{dk}{2\pi}$$

or

$$w(\Delta_n) = \sum_{j=1}^{N} b_j p(\Delta_n - \Delta_j). \tag{11}$$

The coefficients b_j can be determined. Our choice for $P(k)$ leads to equation (12);

$$w(\Delta_n) = \sum_{j=1}^{N} b_j \sum_{m=1}^{M} A_m e^{ik_m(\Delta_j-\Delta_n)}\frac{\sin\kappa(\Delta_j-\Delta_n)}{\pi(\Delta_j-\Delta_n)}$$
$$+ \varepsilon\sum_{j=1}^{N} b_j\delta(\Delta_j - \Delta_n) \tag{12}$$

and the estimator becomes;

$$\bar{W}(k) = P(k)\sum_{j=1}^{N} b_j e^{-ik\Delta_j}. \tag{13}$$

This estimator, called the PDFT estimator (Byrne & Fitzgerald 1984), is a generalization of band-limited extrapolation procedures. The stacking operation now consists of two steps; the coefficients b_j are calculated from equation (12), by means of a damped least-squares inversion with damping factor ε, and then summed with their appropriate kernels $g_j(k)$ in equation (13). Figs 4(c) and (d) show examples of the enhancement of energy in a mode separation diagram, by a broadening of the contours, using equation (13) instead of equation (4). If ε is too small, resolution diminishes. This is illustrated in Fig. 4(d), where mode 5 is unresolved in contrast to Fig. 4(c). Dost (1987) investigated the robustness of the method by tests on a synthetic data set. He concluded that the method produces unbiased results provided that the uncertainty in the *a priori* knowledge, i.e. the width of the boxes in the *a priori* function, is larger than the expected error in the measurements and that the damping parameter ε is not too small.

MEASUREMENTS

Fundamental and higher mode surface wave measurements

Vertical component recordings of the six events of Table 1 have been analysed in order to obtain Rayleigh wave phase velocities. Transverse components were only available in sufficient quantity for two Japanese events. For each event, mode separation diagrams of phase versus group velocity were calculated for 23 frequencies between 20 and 70 mHz. These measurements were obtained in two runs of 14 frequencies, each run with a different group velocity window width, with five overlapping frequencies between 30 and 50 mHz. In this way, the influence of the width of the group velocity window could be checked. Modes, showing up as energy maxima, were automatically picked from the diagrams in the neighbourhood of theoretical values

predicted by the M7 model (Nolet 1977; fig. 10). This model resulted from the inversion of higher mode phase velocity measurements in Europe including the Scandinavian shield and serves as a reference model. Care has been taken that the region searched for a maximum is sufficiently large to rule out any bias by the M7 model. All diagrams were visually inspected to check whether a real maximum is present and not biased by interference effects of neighbouring modes. A first analysis was done without any filtering or weighting to get an impression of the data quality. Then several runs with the PDFT estimator applying different values for the damping parameter were carried out to optimize these results. These data were removed whenever repeated measurements with varying damping parameter produced inconsistent results. Application of the stacking technique assumes a laterally homogeneous sub-surface structure. The path under study does contain some lateral velocity variations (Panza, Mueller & Calcagnile 1980; Spakman 1986; Nolet *et al.* 1986; Snieder 1987). We expect this phenomenon to express itself in a scatter of the measurements.

Rayleigh waves

In order to estimate the reliability of the higher mode Rayleigh wave phase velocity measurements, we calculated vertical component synthetic sections for all six events by

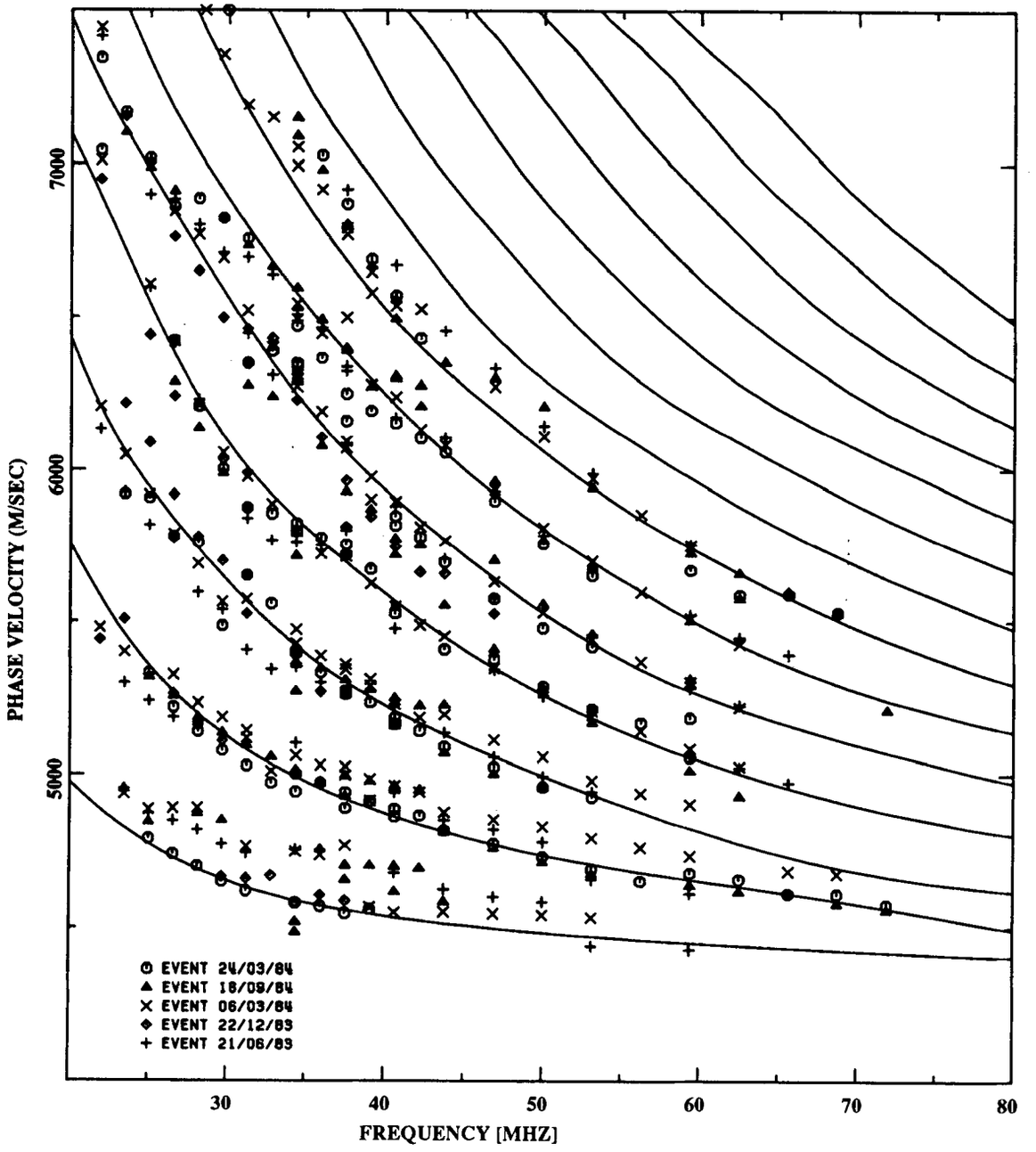

Figure 5. Phase velocity measurements on synthetic seismogram sections. The different mode branches are labelled. Lines indicate theoretical mode branches.

means of mode summation, using mode 1–15 in the frequency range 20–80 mHz. The synthetics were constructed using an earth model from a preliminary analysis (WEPL1; Dost 1986), modified by addition of traveltime information in the inversion procedure. At depths greater than 600 km the PREM model has been adopted. The centroid moment tensor solutions published in the PDE monthly bulletins were used for source information. The results of the analysis of the synthetic sections are displayed in Fig. 5. These measurements have been made without any weighting or deconvolution. From this experiment we make the following conclusions.

(i) The first higher mode cannot accurately be measured, except for the Kurile event (1984 March 24). This may be due to a low excitation of the mode combined with aliasing effects of modes of higher order caused by insufficient station coverage. Identification of the modes becomes more difficult at higher frequencies where group-velocity curves of the various modes approach each other.

(ii) The second and third mode can be determined accurately. It is however necessary to average phase velocities from all events in order to obtain an unbiased result.

(iii) From mode 4 onward only the high-frequency part of the measurements (>40 mHz) produces unbiased results.

With the results from our synthetic experiment in mind, we can now present and discuss the measured phase velocity data set. Rayleigh wave measurements that were judged to be reliable are presented in Fig. 6 [see Dost (1987) for a compilation].

The fundamental mode Rayleigh wave is measured up to 50 mHz. The reason to exclude higher frequencies is that the penetration depth of surface waves decreases with increasing frequency, thus making the surface waves more susceptible to lateral heterogeneity. For the fundamental mode at frequencies higher than 50 mHz this gave rise to an unacceptable scatter in the phase velocity measurements. The fact that the second and third higher modes do not show this large scatter gives us confidence that the deeper structure is much smoother.

The first higher mode shows a large difference in phase velocity between the 1983 June 21 Honshu event and the other events for periods between 20 and 30 mHz. This is also the case for mode 2 and 3. However, the two events in 1983 both suffer from a lack of data in the central part of the array. Since these two events have nearly the same location and very similar moment tensor solutions, an attempt was made to process these events together in one stack. For the first two modes the phase velocities are as a consequence reduced and match the values for the 1984 events between 25 and 30 mHz. Between 20 and 25 mHz this is not the case.

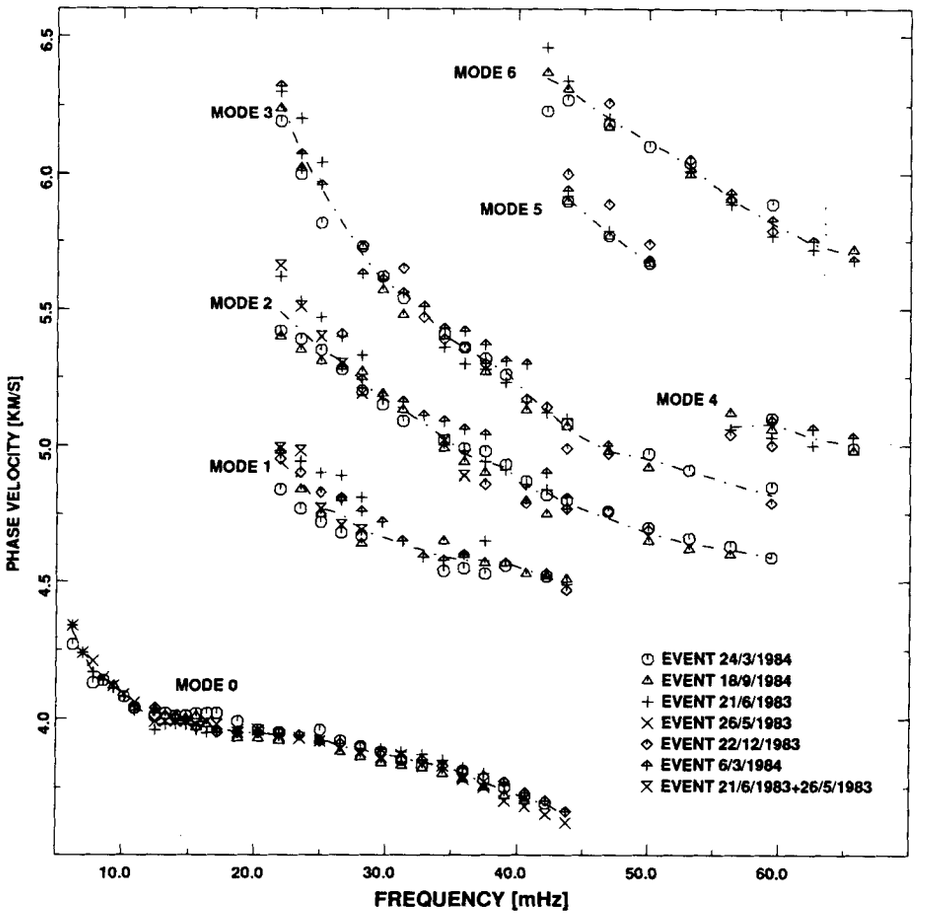

Figure 6. Fundamental and higher mode Rayleigh wave phase velocity measurements. The dashed lines indicate average values used in inversion.

This last period range is at the low-frequency limit of the interval, determined by the total length (aperture) of the array, where we can accurately measure higher mode phase velocities with the NARS array. As a consequence, we did not include phase velocities within the frequency range of 20–25 mHz from the first two higher modes into our data set. It should be noted that this is the period range where there are differences in measurements between Cara *et al.* (1980) and Nolet (1977), who used European WWSSN stations as an array with a much larger aperture than NARS. For modes 4–6 the measurements for period ≥40 mHz are thought to be reliable. Between 20 and 40 mHz strong interference effects play a major role.

The difference between the preliminary data set (Dost 1986) and this final data set is as follows.

(i) The preliminary data were obtained with a simple version of the PDFT estimator. In this version we assumed that all modes are confined to one finite wavenumber band. There was no specific information involved about the modes separately.

(ii) Higher mode measurements were restricted to the frequency range of 30–70 mHz. The new data set is extended to lower frequencies (down to 20 mHz). Higher mode phase velocity measurements for frequencies ≤20 mHz resulted in a large scatter because of the limited length of the array.

(iii) Fundamental mode measurements from Seidl (1971) have been adopted in the preliminary data set. At present they have been substituted by newly measured values. Measurements from 6 to 50 mHz show a good agreement with Seidl's values.

(iv) In the final data set S_n traveltimes are included.

Love waves

An attempt has been made to measure higher mode Love wave phase velocities. Reliable transverse components, measured at at least seven stations, were obtained for the 1984 March 24 Kurile event and the 1984 September 18 Honshu event. Results for the fundamental and first four higher mode phase velocity measurements are shown in Fig. 7. For the fundamental mode the group velocity is also shown. The measurements are compared with a Love wave phase velocity data set by Cara *et al.* (1980). This data set is based on measurements of one Japanese event recorded in western Europe including Scandinavia. In addition, we compare our results with Love wave measurements for North America, based on recordings of two Tonga events (Leveque & Cara 1983).

The fundamental mode shows a continuous dispersion curve for the 1984 March 24 Kurile event, but a jump in phase and group velocity at 25 mHz for the 1984 September 18 Honshu event. The cause of this jump can be recognized from the data (Fig. 8), bandpass filtered between 20 and

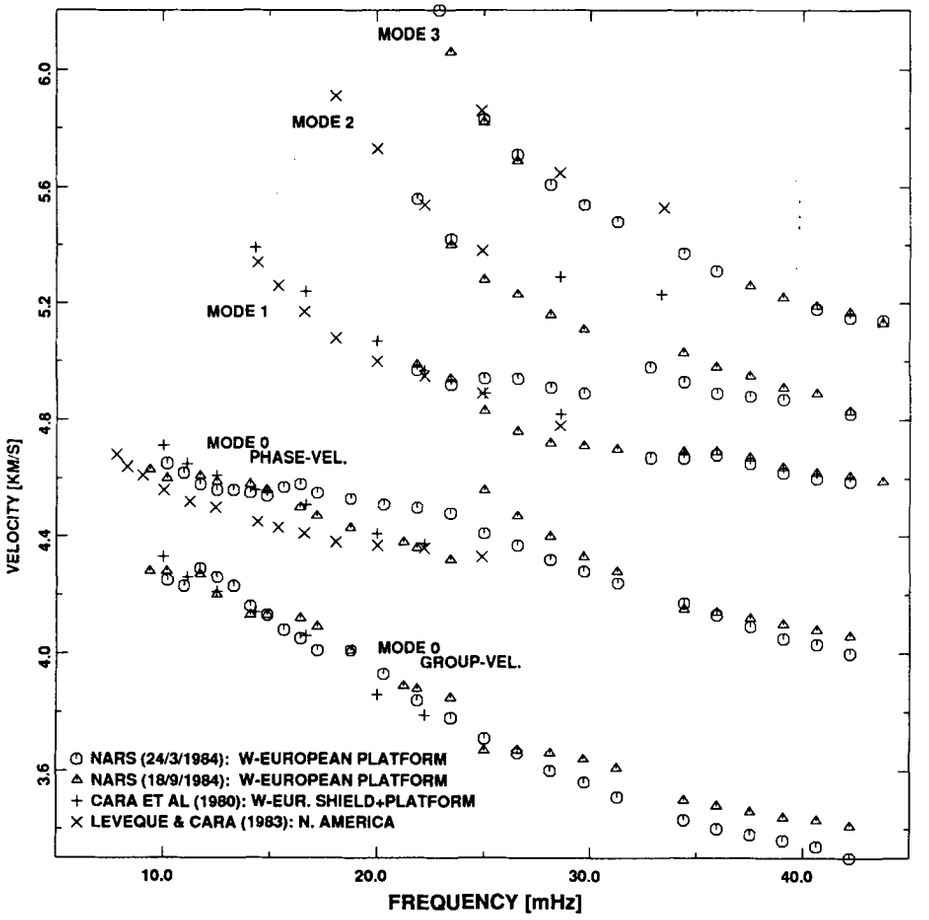

Figure 7. Fundamental and higher mode Love wave phase velocity measurements.

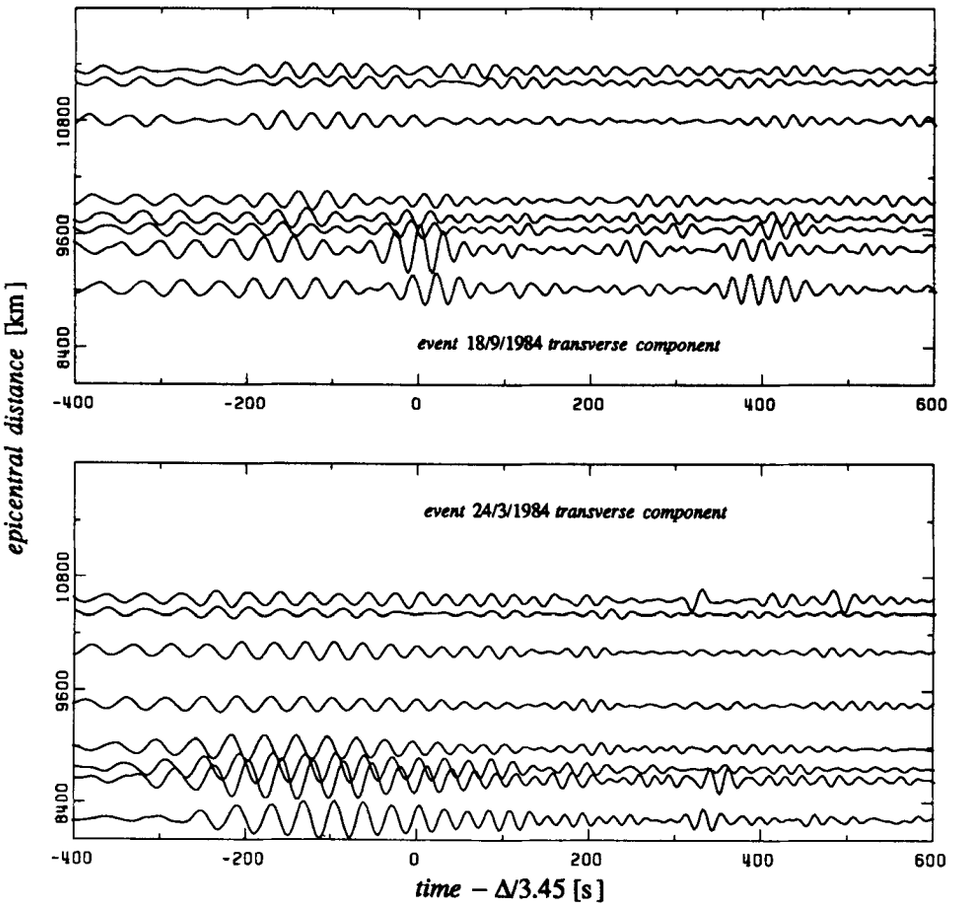

Figure 8. Comparison of transverse components of NARS recordings of the 1984 March 24 and the 1984 September 18 near the fundamental mode Love wave. Time axis is reduced by a factor Δ/3.45.

30 mHz. The Kurile event shows an undisturbed dispersed wavetrain, while the Honshu event shows a beating effect at a group velocity of approximately 3.6 km s^{-1}, the measured group velocity coinciding with the jump in phase velocity. This effect can be caused by multipathing due to lateral heterogeneity. Comparison with fundamental mode phase velocities from Cara *et al.* (1980) shows that their measurements coincide with the results from the Honshu event up to 25 mHz. Unfortunately, their measurements are not extended to higher frequencies and we do not know whether they may be influenced by such a beating phenomenon. North American phase velocities are consistently lower, except in the vicinity of the jump. Again no comparison can be made for frequencies higher than 25 mHz, since no observations have yet been made in that frequency band.

The first higher mode shows a large scatter in phase velocity between 25 and 30 mHz. In the data, the beginning of a S_a phase can be recognized at a group velocity of 4.45 km s^{-1} for the Kurile event, but not for the Honshu event. This can be caused by the greater depth of the Kurile event, which is favourable for the excitation of this phase. The second and third modes show a continuous dispersion curve. Comparison with Cara *et al.* (1980) shows that their second higher mode phase velocities are influenced by interference effects of the second and third modes. The phase velocities for Northern America are close to our measurements.

Because of the very limited data set and the anomalous features in the determination of the phase velocities just described, we decided to await more accurate measurements rather than to invert simultaneously for Love and Rayleigh wave phase velocities.

Traveltimes

S_n traveltimes from selected European events provide an additional independent source of information about the upper mantle shear velocity structure that can be included in the inversion procedure. The S_n wave has been interpreted in many ways, including a head wave refracted at the base of the Moho, but Mantovani *et al.* (1977) show that an interpretation as a wave that is guided by the lithosphere travelling with a constant apparent velocity is more appropriate. The S_n phase can be interpreted as a lid-wave for shallow focal depths and a model containing a low-velocity zone with energy confined to the uppermost few tens of km of the mantle.

Previous studies have incorporated shear wave traveltimes for the European continent. Lehmann (1961) compiled *S* readings and demonstrated the existence of a low-velocity layer in Europe down to 220 km depth. Mayer-Rosa &

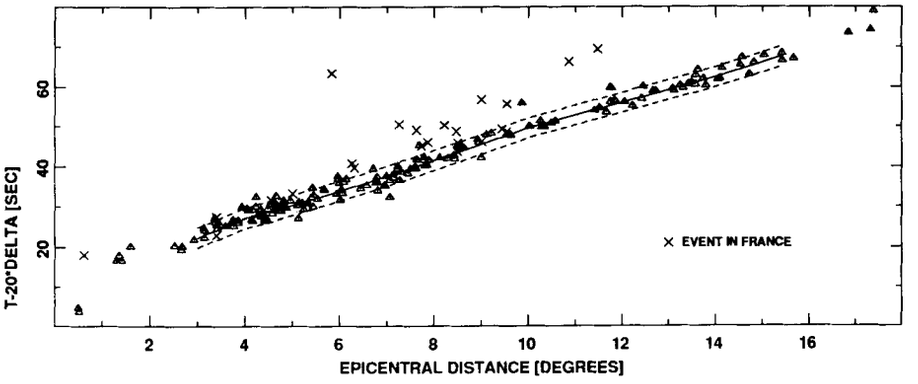

Figure 9. Reduced S_n traveltime as a function of epicentral distance. The solid line represents the inferred traveltime curve, dashed lines the assumed standard deviation. Data from two French events are marked by a cross instead of a triangle and are not used in the construction of the traveltime curve.

Mueller (1973) examined P and S times together with fundamental mode Rayleigh waves and concluded that in the upper 200 km a clear distinction could be made between eastern and western Europe.

Regional S arrivals are difficult to read and may show considerable scatter. In particular, too-large arrival times are to be expected due to a larger amplitude SS_n phase that arrives after the S_n phase (Kennett 1985). We tried to infer a traveltime curve for selected events and stations that sample the structure under NARS using ISC bulletins as a database. To minimize the influence of lateral heterogeneity, we neglected events in eastern Europe and events in Algeria and southern Spain because of anomalous S_n velocities (Panza *et al.* 1980; Spakman 1986). The data set contains mainly events in the North Sea, United Kingdom, Belgium and the Netherlands. The inferred traveltime curve (Fig. 9) is compatible with the majority of the data. A scatter in the measurements between 5 and 12° is mainly due to two French events. In general, regional French events give a large scatter in S_n traveltimes and are thus omitted. An average standard deviation in the traveltime curve of ±2.5 s (Fig. 9) is representative of the data set.

INVERSION

The data set was inverted using an extension (Kennett & Nolet 1978; Nolet 1978) of the generalized inversion technique (Wiggins 1972). Dispersion data and traveltime data are inverted simultaneously. The inversion method is based on the linear or linearized relationship between perturbations $p(r)$ in a starting model and the resulting change in the data c_i;

$$c_i = \int_0^a G_i(r)p(r)\,dr. \tag{14}$$

The starting model is discretized and consists of a stack of horizontal constant velocity layers of varying thickness. Using parameters p_k and known smooth interpolation functions $h_k(r)$ we can describe the perturbation as $p(r) = \sum_{k=1}^{N} p_k h_k(r)$. The formulation of the inversion problem can then be reduced to a set of matrix equations;

$$c_i = G_{ik}p_k, \qquad i = 1, \ldots, M \tag{15}$$

where

$$G_{ik} = \int_0^a G_i(r)h_k(r)\,dr. \tag{16}$$

In general $N < M$ and (14) can be solved by minimizing $|c_i - G_{ik}p_k|^2$, leading to Gauss normal equations

$$\mathbf{G}^T\mathbf{G}p = \mathbf{G}^T c. \tag{17}$$

If N is not too small, $\mathbf{G}^T\mathbf{G}$ is an ill-conditioned matrix and small errors in the data may blow up to large errors in the solution vector p. Therefore we use a generalized inverse of $\mathbf{G}^T\mathbf{G}$. Suppose $N - K$ eigenvalues of $\mathbf{G}^T\mathbf{G}$ are equal to zero, we can diagonalize and truncate the matrix;

$$\mathbf{G}^T\mathbf{G} = \mathbf{V}\boldsymbol{\Lambda}\mathbf{V}^T, \tag{18}$$

where $\mathbf{V}$ is a $N \times K$ matrix whose columns form the first K eigenvectors of $\mathbf{G}^T\mathbf{G}$ and $\boldsymbol{\Lambda}$ the $K \times K$ diagonal matrix of non-zero eigenvalues. $\boldsymbol{\Lambda}$ contains eigenvalues in sorted order ($\lambda_1 > \lambda_2 > \lambda_3 \ldots > \lambda_k$). Combination of (16) and (17) leads to a truncated system of matrix equations that can be solved. If we now choose to find a model that is closest to the starting model, we can find a local average $\langle p \rangle = \mathbf{R}p$, where $\mathbf{R} = \mathbf{V}\mathbf{V}^T$ and the variance in the model parameters is given by $\mathrm{var}(p_k) = \sum_{j=1}^{N} V_{kj}^2/\lambda_j$. Small eigenvalues introduce a large variance in the model parameters and therefore not only zero-valued eigenvalues, but also all $\lambda_j < \sigma_{\max}^{-2}$, where $\sigma_{\max}$ is the standard deviation, are neglected. This criterion is known as a 'sharp cut-off' criterion and is applied in the present inversion. The number of eigenvectors used in the inversion determines the trade-off between depth resolution and variance in the model parameters. The method allows the construction of models that fit the data. However, these models are non-unique due to the finite nature of the data set and the errors in the measured data.

S velocity, v_S, and density, ρ, were inverted simultaneously after they had been weighted with *a priori* uncertainty. P velocity, v_P, was treated as coupled to v_S with a fixed Poisson's ratio. This is convenient since only the fundamental mode is weakly sensitive to v_P. One should keep in mind that surface waves are only sensitive to

changes in the gradient of the density, not to absolute changes (Nolet 1977). As an extra constraint, no change in surface gravity is allowed to result from the inversion. As a measure of the fit of a model to the data, relative residuals are calculated. This is the average root mean square of the difference between observed and calculated values (ξ) for the data divided by the standard error. For N data, ξ corresponds to $(\chi^2/N)^{1/2}$ with χ^2 the familiar statistical quantity 'chi-square'. Since $N \gg K$, the number of eigenvectors used in the construction of the model, the number of degrees of freedom is approximately N. Thus, when $\xi < 1$ a model has been chosen that fits the errors in the data rather than the trend in the data. On the other hand, if $\xi > 1$ a poor fit between the data and the model is obtained. Therefore we should aim at a relative residual $\xi = 1$. Statistical techniques can be used to decide whether the addition of an extra eigenvector is warranted by the data. We found it much more convenient to decide subjectively whether we are near enough to $\xi = 1$ and to avoid model features of doubtful reality. We shall make up for this by applying resolution analysis *a posteriori*. Resolution is calculated by introduction of constant velocity changes over thick layers, thereby forcing the system to be over-determined. The inversion then gives the variance in the model averaged over the specified layer thickness.

Data errors play an important role in the inversion procedure and have been estimated carefully. Each phase velocity measurement used in the inversion is the result of averaging over all analysed events. Measurements of individual events are averaged values of multiple mode diagram readings, using different filter parameters. Comparison with measurements on a synthetic data set, as discussed previously, gives confidence in the estimated errors. The standard deviation for the fundamental mode phase velocities is in the range 0.01–0.03 km s^{-1}, higher mode phase velocities 0.02–0.07 km s^{-1}, sometimes even reaching 0.11 km s^{-1}. Since errors in the traveltime values can be introduced by errors in the estimated origin time and location of the events, S_n traveltime values for 14 different European events are used in the analysis, averaging out any systematic errors. Care has been taken to ensure that great-circle paths cover the entire area under investigation.

The inversion procedure requires a starting model. One should be cautious not to influence results with *a priori* assumptions, e.g. a low density or velocity channel in this starting model. A further issue is that of possible anisotropy, since the M7 model is an isotropic model. Cara *et al.* (1980) observed a possible anisotropy under western Europe, based on the incompatability of Love and Rayleigh wave phase velocities. Mitchell (1984) mentions as possible alternative explanations for a Love/Rayleigh incompability a laterally varying structure or a failure to include a sufficient number of layers in the inversion process. Since there is at present no adequate Love wave data set at hand for the west-European platform, we interpret our data assuming an isotropic model.

Nolet's data sample the Baltic shield and the west-European platform, while our new data sample only the platform structure. Inversion of the two data sets, using the same starting model enables us to construct a shield model. Differences in shear velocity and density can thus be investigated.

Inversion for the west-European platform

In a preliminary inversion (Dost 1986), we took a modified M7 model as the starting model. The M7 model does not exhibit sharp discontinuities near 400 and 670 km depth, since the higher mode data set used in its construction could not distinguish between a sharp or smooth feature at those depths. The shear velocity under the Moho down to 220 km depth was set to a constant 4.45 km s^{-1} and density to 3.4 g cm^{-3}. We restricted density variations in this depth interval to 0.2 g cm^{-3} in order to obtain realistic results. In the resulting preferred model (WEPL1) the most remarkable features are a broadening of the low-velocity zone and the disappearance of a Lehmann discontinuity. In addition, a high shear velocity lid between 80 and 120 km was found to correlate with a high density. In the present inversion, with a more refined data set, we investigate the influence of the starting model on the inversion results. First the new data set is inverted with the same smooth starting model as WEPL1, then we investigate the influence of sharp discontinuities at varying depths on the inversion result.

Inversion with a smooth starting model

Figure 10 shows a comparison of the inversion results (WEPL1a) using the modified M7 model as starting model. In the same figure WEPL1 is reproduced. Incorporation of traveltimes (WEPL1a) results in a more pronounced high shear velocity lid and low shear velocity layer. The Lehmann discontinuity at 220 km depth is absent in both models. Even if the Lehmann discontinuity is present in the starting model, it is removed by the inversion procedure. The average shear velocity between 350 and 650 km is 0.1 km s^{-1} higher in WEPL1a than in WEPL1. It is remarkable that the density high at 100 km depth disappears completely whereas the density high around 200 km depth remains. The question of whether this density feature is resolved or not arises. Resolution calculations show that the standard deviation of the shear velocity v_S is comparable for both models. The standard deviation of the density, however, behaves differently. The WEPL1a model has a worse resolution than WEPL1 (Dost 1987). Thus the density high at approximately 200 km depth is not resolved and as a consequence ξ will not change when the density curve is smoothed. Comparison of the model fit to the data for WEPL1a and for a model with a smooth density curve between 100 and 300 km depth, however, points towards the existence of the density high; ξ is reduced from 1.69 to 1.38, which is significant. This disagreement between resolution calculations and the model fit to the data can be caused by violation of the linearity assumption in the inversion. Experiments show that the thickness of the high-velocity lid determines the resolution in the density; a smaller lid thickness results in an improvement in resolution. It is interesting to note that Lerner-Lam (1985) reports that lid thickness can be substantially reduced by allowing a transverse isotropic parametrization of velocity in the inversion. In our present inversion this is not accounted for.

Finally, we tested the correlation between v_S and ρ at 100 km depth, suggested by WEPL1, by coupling v_P, v_S and ρ by Poisson's ratio and Birch's law in the inversion. The

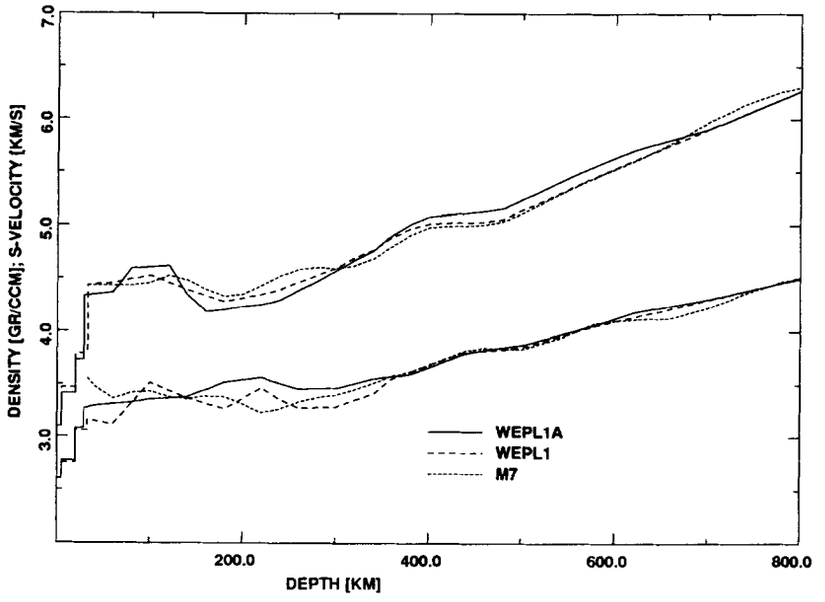

Figure 10. Density (lower curve) and shear velocity as a function of depth.

resulting shear velocity exhibits the high-velocity lid, but the density does not show the high observed in WEPL1.

In all cases the model fit to the data shows a trade-off between the fundamental mode data from 90 to 160 s and higher mode data. Mode 5 cannot be adequately fitted; the measured phase velocities are always too low, due to interference with the 4th and 6th higher modes.

Inversion with a starting model containing sharp discontinuities

For a starting model containing sharp discontinuities, we took the modified M7 model down to 360 km depth and PREM (Dziewonski & Anderson 1981) at greater depths. In a first experiment the influence of a possible Lehmann discontinuity is investigated. Three starting models were used: one with a smooth gradient between 200 and 300 km depth, one with a strong gradient between 220 and 240 km depth and one with a first-order discontinuity at 220 km. The results are displayed in Fig. 11. All models, built with nine eigenvectors, fit the data equally well ($\xi = 1.44$, 1.44 and 1.42). Since these values are comparable with results from inversions with a smooth starting model, we conclude that the existence of a Lehmann discontinuity is not resolved by our data set. In general, the pronounced density high at 200 km depth, present in inversions with a smooth starting model, disappears. An increase in density from 40 to 100 km depth is resolved for all models. For a starting

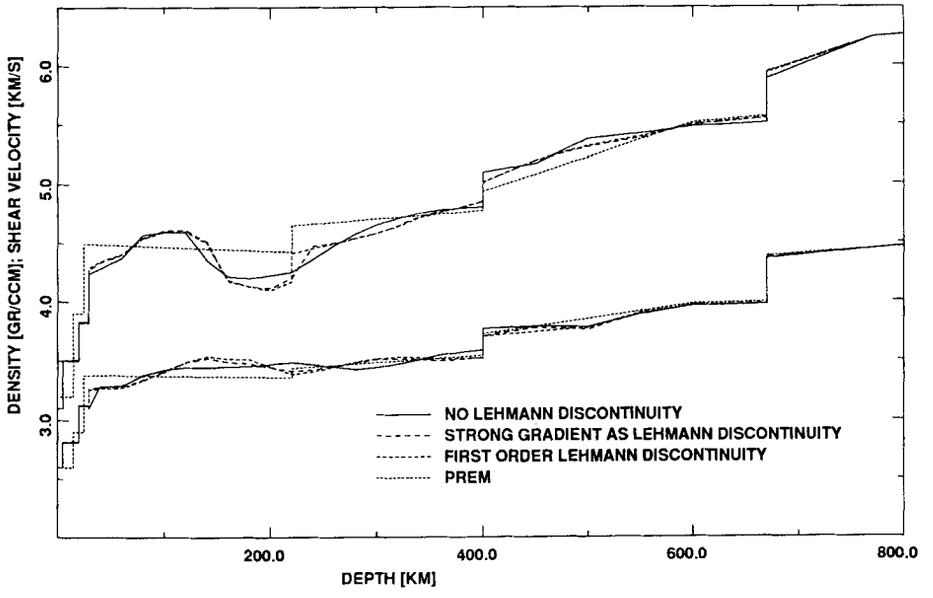

Figure 11. Denstiy (lower curve) and shear velocity as a function of depth for starting models with discontinuities at 400 and 650 km depth. Inversion results for three different starting models are compared with PREM.

model with a constant density from 40 to 300 km depth, the density gradient is always introduced and results in a significant improvement of the fit to the data. This agrees with the WEPL1 model, although the density gradient is now smoother. Variations in thickness of the high-velocity lid do not affect resolution in density, as was the case in the inversion with a smooth model. Models with a Lehmann discontinuity exhibit a thicker high-velocity lid and a more pronounced low-velocity layer. Although the inversion of phase velocities and traveltimes cannot distinguish between the different models, these pronounced models fit the traveltimes better than less pronounced models and are thus preferred. The '400' km discontinuity starts for all models at higher shear velocity values than PREM. The model without a Lehmann discontinuity exhibits a jump in shear velocity about 1.8 times larger ($\Delta v_S = 0.3\,\mathrm{km\,s^{-1}}$) than PREM ($\Delta v_S = 0.17\,\mathrm{km\,s^{-1}}$) and approximately 1.3 times larger than the two models containing a Lehmann discontinuity ($\Delta v_S = 0.23\,\mathrm{km\,s^{-1}}$). To our knowledge, the only published global or regional model with a comparable velocity contrast at the '400' km discontinuity is the EPR-B model for the mantle under the East Pacific Rise (Wielandt & Knopoff 1982). However, the depth of the discontinuity in this model is much larger (465 km). The average shear velocity of all three models between 400 and 600 km is significantly higher than PREM. Resolution of v_S and ρ is approximately the same as in WEPL1a.

The disappearance of the density anomaly at 200 km depth and the disappearance of the dependence of density resolution on lid thickness demonstrate the importance of the existence of discontinuities in the starting model. No explicit assumptions about anisotropy or a density high at 200 km depth are needed to obtain an acceptable model. The departure from smooth models in the linearized inversion may introduce non-linear effects. The presented resolution calculations should therefore be interpreted as a rough order-of-magnitude calculation. We can conclude that, although the Lehmann discontinuity is not resolved, a smooth gradient between 200 and 400 km depth leads to a large jump in shear velocity at the '400' km discontinuity compared to a reference earth model like PREM and more regional models.

We next investigate the influence of the depth of the two major discontinuities in the inversion. The depth of the 400 km discontinuity, best determined by body wave studies, ranges from 380 to 420 km depth. In general the sharpness of this discontinuity is not very accurately determined, except in northern Australia where a first-order discontinuity at 406 km has been found (Leven 1985). However, it must be sharp enough to produce converted body wave phases visible on stacks of short-period records (Paulssen 1988). We investigate three starting models with a first-order discontinuity at 380, 400 and 420 km depth respectively, as well as a model with a strong gradient between 380 and 420 km depth. Results for the first three models are displayed in Fig. 12. For the model with a discontinuity at 380 km depth, the Lehmann discontinuity disappears, and the jump in v_S at the discontinuity becomes larger ($0.28\,\mathrm{km\,s^{-1}}$) than in PREM ($0.16\,\mathrm{km\,s^{-1}}$). For the models with a discontinuity at 400 and 420 km depth the jump in shear velocity at the discontinuity is approximately $0.22\,\mathrm{km\,s^{-1}}$, comparable to existing regional models like SNA and TNA (Grand & Helmberger 1984). The gradients in shear velocity between the '400' km discontinuity and 600 km depth are approximately equal for the three models. There is no resolved difference in density gradient for the three models. An inversion with a starting model exhibiting a strong gradient in shear velocity and density between 380 and 420 km depth gave similar results as the models with a discontinuity at 400 and 420 km depth. This observation again shows the inability of the surface wave data to discriminate between a strong gradient and a first-order

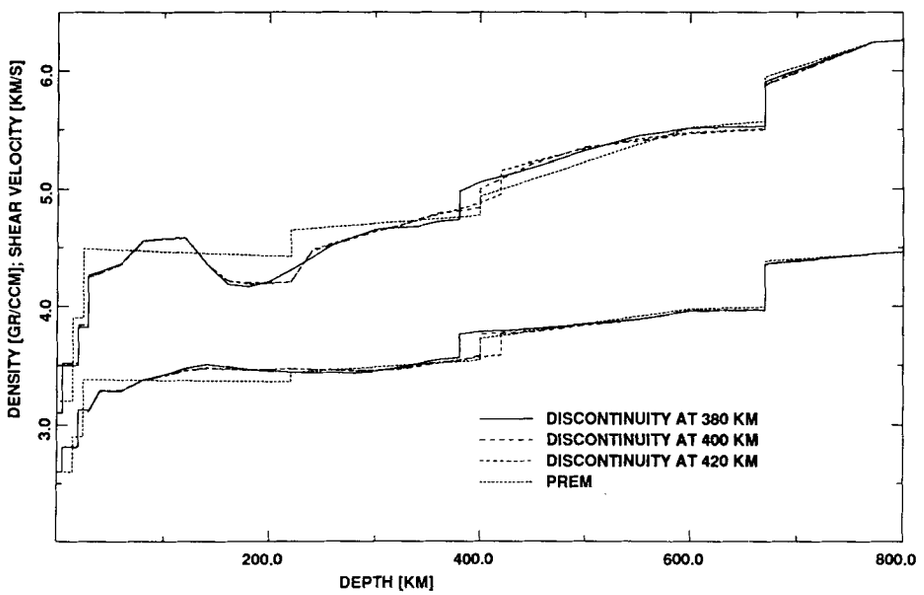

Figure 12. Density (lower curve) and shear velocity as a function of depth for a starting model with the '400 km' discontinuity at 380, 400 and 420 km depth. Inversion results for three different starting models are compared with PREM.

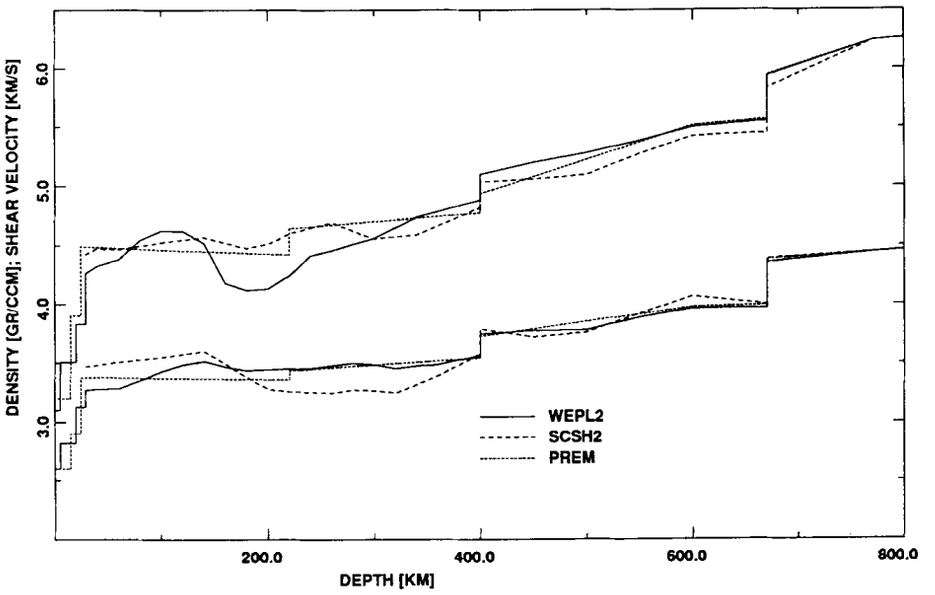

Figure 13. Density (lower curve) and shear velocity as a function of depth for WEPL2 and SCSH2. For comparison PREM is shown.

discontinuity. The influence of the location of the 650 km discontinuity on more superficial gradients in shear velocity or density of the model is negligible.

There is a difference in the width of the high-velocity lid and absolute depth of the low-velocity layer between the inversion results in Figs 11 and 12. As stated before, models with a thicker high-velocity lid and more pronounced low-velocity layer best fit the traveltime data and are thus preferred. The use of models with a more pronounced velocity contrast and thicker high-velocity lid instead of those shown in Fig. 12 has no influence on our conclusions.

For a definite choice of an average platform model we include constraints from body wave studies. Paulssen (1987 and personal communication) studied *P*- and *S*-waveforms from European events using NARS recordings and WKBJ modelling. She found that waveforms from different source–receiver paths could not be modelled by one homogeneous model down to a depth of at least 450 km, and that bounds on the depth of the '400' km discontinuity can be only roughly specified. A minimum depth of the '400' km discontinuity of 400–420 km is constrained from this modelling.

Our final model for the west European platform (WEPL2; Fig. 13, Table 2) thus consists of a high shear velocity lid from 80 to 140 km depth, a pronounced low-velocity channel from 140 to 240 km depth and a smooth gradient in velocity between 240 and 400 km depth. The two major discontinuities are placed at 400 and 650 km depth. The density shows a steep gradient between 60 and 140 km depth, followed by an approximately constant value down to 300 km depth. At greater depth, density follows PREM closely. The resolution is indicated in Table 3.

Table 2. WEPL2.

depth [km]	v_s [km/s]	ρ [gr/ccm]	depth [km]	v_s [km/s]	ρ [gr/ccm]
0-5	3.100	2.600	320	4.647	3.453
5-20	3.509	2.815	340	4.736	3.473
20-29	3.829	3.128	360	4.783	3.487
29	4.263	3.271	380	4.830	3.527
40	4.323	3.281	400	4.876	3.564
60	4.382	3.283	400	5.096	3.745
80	4.543	3.351	450	5.202	3.773
100	4.622	3.428	500	5.282	3.774
120	4.622	3.487	550	5.384	3.886
140	4.520	3.516	600	5.502	3.964
160	4.178	3.466	635	5.529	3.965
180	4.117	3.435	670	5.556	3.966
200	4.130	3.444	670	5.940	4.345
220	4.244	3.453	721	6.087	4.399
240	4.414	3.455	771	6.241	4.443
260	4.453	3.477	871	6.311	4.504
280	4.505	3.499	971	6.378	4.563
300	4.557	3.484			

Table 3. Resolution WEPL2.

depth [km]	v_s [km/s]	st dev [km/s]	layer thickness [km]	depth [km]	ρ [gr/ccm]	st dev [gr/ccm]	layer thickness [km]
40	4.323	.076	40	40	3.281	.170	40
100	4.625	.091	80	100	3.428	.170	80
180	4.117	.056	80	180	3.435	.210	80
260	4.453	.110	80	260	3.477	.210	80
340	4.736	.078	80	340	3.473	.220	80
440	5.181	.092	120	440	3.767	.240	120

In all inversions presented here there is a trade-off between the misfit of fundamental mode data at 90 to 160 s and higher mode data, as noted for the inversion with a smooth starting model. A period of 90 s for the fundamental mode corresponds to a penetration depth of approximately 180 km, the deepest part of the low-velocity zone. Thus the region around the possible Lehmann discontinuity is badly resolved in the inversion, due to incompatibility between fundamental and higher modes. The bias of the fifth mode also remains present.

Inversion for the Baltic shield

We compared our data set sampling the west-European platform with Nolet's data set for western Europe including Scandinavia, to detect differences in structure between the two regions. Although our measurements are for much higher frequencies, this comparison gives information on gross differences. We therefore compared smooth models inverted with only a limited number of eigenvectors. Nolet's phase velocity data were reinverted using the same starting model as in the WEPL2 inversion. A smooth model could be obtained with seven eigenvectors and shows basically the

Table 4. SCSH2.

depth [km]	v_s [km/s]	ρ [gr/ccm]	depth [km]	v_s [km/s]	ρ [gr/ccm]
29	4.423	3.469	340	4.589	3.317
40	4.473	3.483	360	4.664	3.392
60	4.466	3.509	380	4.739	3.483
80	4.496	3.529	400	4.814	3.575
100	4.525	3.549	400	5.034	3.787
120	4.546	3.574	450	5.057	3.718
140	4.567	3.601	500	5.093	3.755
160	4.520	3.492	550	5.277	3.921
180	4.475	3.382	600	5.421	4.065
200	4.511	3.281	635	5.437	4.031
220	4.597	3.259	670	5.451	3.998
240	4.650	3.253	670	5.836	4.387
260	4.692	3.246	721	6.035	4.415
280	4.623	3.272	771	6.241	4.443
300	4.553	3.266	871	6.311	4.504
320	4.571	3.246			

same features as M7 (Fig. 10). A minimum in density around 220 km depth is retained. The new data were reinverted to obtain a smooth seven-eigenvector model for comparison. Traveltimes have been excluded. The shield model was calculated by means of the expression;

$$\vec{m}_s\Delta_s = (\Delta_p + \Delta_s)\vec{m}_{s+p} - \Delta_p\vec{m}_p \qquad (19)$$

where Δ_s and Δ_p stand for the path length over the shield and the platform structure respectively and $\vec{m}_s$, $\vec{m}_p$ and $\vec{m}_{s+p}$ denote shield, platform and averaged model values. The resulting model, SCSH2, is tabulated in Table 4. A comparison between SCSH2 and WEPL2 is shown in Fig. 13. The approximate constant shear velocity value at 50–300 km depth that was found in preliminary results is still present in SCSH2. The latter model shows more fluctuations between 220 and 300 km depth, but this can be attributed to the region where resolution becomes bad in WEPL2 and the possible existence of a Lehmann discontinuity is not resolved. This observation that the low-velocity channel is absent under the Baltic shield is also supported by Calcagnile's (1982) regionalization of fundamental mode Rayleigh wave phase velocities. Between 400 and 500 km depth, a difference in shear velocity between WEPL2 and SCSH2 is observed. For the density, an average 0.2 g cm^{-3} difference between 200 and 320 km depth is observed. As noted before, resolution calculations can only be used as a rough estimate. In these model difference calculations, this becomes even more troublesome. However, since the density difference is spread out over at least 120 km depth and the estimated resolution for WEPL2 at 260 km is 0.21 g cm^{-3} over 80 km depth, it is acceptable to conclude that there is a strong indication for a difference in density between the Baltic shield and the west-European platform between 200 and 350 km depth.

INTERPRETATION AND CONCLUSIONS

Interpretation of the models in terms of mantle mineralogy requires information about elastic constants and their pressure and temperature derivatives. Recently progress has been made in the measurement of these parameters in high-pressure laboratories. However, tests of different hypotheses for upper mantle structure have not yet produced decisive arguments in favour of any proposed theory. These hypotheses are mainly based on arguments about the average mineralogy (pyrolite and piclogite models), but may include arguments concerning mechanical properties (tectosphere model or lithospheric doubling concept). We briefly review the major hypotheses, compare our shear velocity and density models with models constructed from recently published laboratory data and discuss the implications for the west-European platform and Baltic shield structure. An interpretation of preliminary surface wave results in terms of mineralogy was published in Nolet *et al.* (1986b).

Mineralogical models

Pyrolite

Ringwood (1975, 1979, 1982) proposes a model for the upper mantle based on a homogeneous undepleted mantle mineral assembly; pyrolite (Table 5). Pyrolite is assumed to be the primitive source material of basalts, formed upon partial melting. Different basalt types are the result of a difference in the percentage of partial melting (nephelinites, 1–5 per cent; alkali basalts, 5–10 per cent; tholeiites, 15–25 per cent; and komatiites, 30–60 per cent). The remaining fractions after partial melting are garnet and spinel lherzolite, complementary to nephelinites and alkali basalts, harzburgite, complementary to tholeiites and dunite, complementary to komatiites. The discontinuities at 400 and 650 km depth are interpreted as phase changes. The '400' km discontinuity is interpreted as the transition from olivine to modified spinel (β-phase) accompanied by an increasing solid solution of pyroxene in garnet. The transition zone, the region between 400 and 650 km depth, is mainly consistent with a modified spinel plus garnet composition with minor clinopyroxene. The latter phase exists down to 500 km depth. At 550 km depth the modified spinel transforms to spinel (γ-phase), which breaks down to perovskite and periclase between 650 and 700 km depth. Garnet breaks down to the ilmenite structure starting at 600 km depth. A subducting slab, mainly consisting of a basaltic upper layer underlain by a harzburgite layer, sinks to approximately 600 km depth and remains denser than the surrounding mantle. Below 650 km depth the former basaltic layer remains denser, but the harzburgite layer becomes relatively buoyant and material gathers at the 650 km discontinuity. This material is heated by thermal conduction and the former basaltic crust is subjected to partial melting. As a result the former harzburgite is fertilized, becomes buoyant and starts forming diapirs into the upper mantle. The residual former basaltic layer sinks as large blocks into the lower mantle in a dense perovskite structure.

Piclogite

Anderson (1979a), Oxburgh (1980), Bass & Anderson (1984) and Anderson & Bass (1984, 1986) discuss the piclogite model based on a chemically inhomogeneous mantle composition. It is assumed that an original melt layer or magma ocean was present. The scenario envisages

Table 5. Comparison of models used in hypothesis testing.

	Pyrolite			Piclogite		
Comp.	Bass & And. [wt %]	And. & Bass [wt %]	Weidner [vol %]	Bass & And. [wt %]	And. & Bass [wt %]	Weidner [vol %]
Ol	57	57	61	16	16	16
Opx	17	17	15	3	6	3
Cpx	12	12	10	44	33	45
Gt	14	14	14	37	45	36

low-density olivine crystallizing and becoming concentrated in the shallow mantle in peridotite. Garnet crystallizes later and sinks, while the residual fluid freezes to a clinopyroxene–garnet rich mixture with some olivine. This residual is called piclogite (or an olivine eclogite) and is compositionally close to komatiite. Pyroxene dissolves with increasing depth in the garnet and at the bottom of the transition zone (550–650 km) garnetite is formed. Eclogite will accumulate at the 650 km discontinuity, as it cannot penetrate the discontinuity because of the high density of the Al_2O_3-poor assemblages below. In this way a stratification of the upper mantle is achieved. From top to bottom the upper mantle thus consists of basalt, peridotite and eclogite. Basalt injected into the mantle during subduction inverts at shallow depths to eclogite and sinks rapidly through the mantle.

Anderson (1979a, b) interprets the 220 km discontinuity as the boundary between the peridotite and eclogite layer and the 400 km discontinuity as the boundary between eclogite and garnetite. More recently Liu (1980) and Bina & Wood (1984, 1987) have argued that the eclogite to garnetite transition would not produce the observed 400 km discontinuity. As a result Anderson & Bass (1984, 1986) and Bass & Anderson (1984) moved the boundary between peridotite and eclogite down from 220 to 400 km depth. Most remarkable is the difference in piclogite composition between the Bass & Anderson (1984) and Anderson & Bass (1984) paper. A comparison between compositions used by different authors is complicated by the use of both weight and volume percentages by these authors.

Hypothesis testing

In a recent series of articles, partly reviewed by Anderson & Bass (1986), the pyrolite and piclogite models are tested against global seismological results [the PREM model of Dziewonski & Anderson (1981)]. As a data base, an internally consistent data set of laboratory measurements on a pyrolite composition by Akaogi & Akimoto (1977, 1979) is widely used. A review by Jeanloz & Thompson (1983) gives valuable information on existing data and uncertainties. The only laboratory measurements on a piclogitic composition has been made by Irifune *et al.* (1986) and Irifune & Ringwood (1987), who studied an alkaline-poor olivine tholeiite.

Acoustic velocities are calculated at depth by projection along adiabats. This assumption of adiabaticity is thought to be reasonable for the deeper part of the upper mantle. In terms of thermodynamics the mineral assemblage is heated isobarically up to the 'foot' to the adiabat temperature. From there it is adiabatically compressed to the desired pressure (Weidner 1986). Bass & Anderson (1984) and Anderson & Bass (1984) compared pyrolite and piclogite composition in this way, using PREM as a reference model. They concluded that both the pyrolite and piclogite models are acceptable down to the 400 km discontinuity, but that for the transition region between 400 and 650 km depth the pyrolite model generates too-high shear velocity values, while piclogite is appropriate. Anderson & Bass (1984) show that, for shields, the observed velocities are close to those predicted assuming a 1400 °C adiabat for depths greater than 200 km. Other models, e.g. tectonic rise, approach this adiabat at much larger depths (near 400 km). In contrast Weidner (1985, 1986), Bina & Wood (1984, 1987) and Akaogi *et al.* (1987) reach the opposite conclusion, that the pyrolite model is acceptable, and note that the different results are due to different assumptions concerning phase equilibria for the pyroxene–garnet transformation, elastic properties of the majorite phase and pressure and temperature derivatives of the elastic properties of the high-pressure phases. In Weidner's (1985, 1986) studies, a 1400 °C foot to the adiabat has been used as well. Irifune *et al.* (1986) conclude that, based on measured properties of a piclogite-like composition, the piclogite model cannot explain the velocity jump at 400 km depth and the high gradient in the transition zone.

The most important parameters that lead to the present controversy are the jump in shear velocity at the 400 km discontinuity, the velocity gradient in the transition region (400–650 km depth) and the absolute level of velocity between 300 and 400 km depth. In the following we will describe these in detail.

Absolute velocity 300–400 *km depth*

In this region all calculated models give more or less the same results. Here the assumption of the 1400 °C foot to the adiabat is only valid for shields.

400 *km discontinuity*

Bass & Anderson (1984) assume that at 400 km depth all olivine is transformed to modified spinel (β-phase) and that all orthopyroxene is already dissolved in garnet as majorite. Their pyrolite model therefore creates a jump in velocity that is twice the observed value whereas piclogite, which contains less olivine, produces the correct velocity jump due to the additional pyroxene to garnet transition. Bina & Wood (1984) demonstrate, both on experimental and thermodynamical grounds, that the eclogite–garnet transition does not exhibit any discontinuity in bulk sound velocity from 11 to 23 GPa. Weidner (1985) argues that the magnitude of the 400 km discontinuity is sensitive both to the amount of olivine in the mantle, and to the yet unmeasured pressure derivative of the shear modulus of the high-pressure phase. He finds the observed velocity and density jump consistent with 40–65 volume percentage olivine. For models with a smaller olivine content, an accompanying chemical discontinuity should be present. The contradition with findings by Lees, Bukowinski & Jeanloz (1983), that *P*- and *S*-wave velocities are inconsistent with a pyrolite mantle, are attributed to incorrect elastic parameters for spinel and modified spinel and differences with Bass & Anderson (1984) in phase relations and properties of the garnet phase. Subsequently Weidner (1986) argues that some observations are incompatible with Bass & Anderson's conclusions. He criticized the assumption that Ca-poor pyroxene dissolves completely into the garnet phase around 400 km depth, arguing that Akaogi & Akimoto (1977; 1979) over-estimated the pressure for a complete dissolution of Ca-poor pyroxene. Irifune *et al.* (1986) and Akaogi *et al.* (1987) report that this is the case. A result of the over-estimation of pressure should be a considerable solution of pyroxenes into garnets at depths as

shallow as 200 km. The recent discovery by Moore & Gurney (1985) of pyroxenes in solid solution with garnets as inclusions in diamonds from kimberlites supports these conclusions. Akaogi *et al.* (1987) present new phase diagrams of the pyroxene–garnet transformation, based on thermochemical data, and compare results with experimental data from Akaogi & Akimoto (1977), where pressures above 13 GPa are reduced. Calculated boundaries match the results of the experimental runs in general, while the maximum solubility of $Mg_4Si_4O_{12}$-pyroxene in garnet at 1000 °C is significantly larger than the value determined by Akaogi & Akimoto (1977). Akaogi *et al.* (1987) conclude that Ca-poor pyroxene gradually dissolves in garnet, resulting in a complete dissolution at about 450 km depth. Also, they tentatively assume that Ca-rich pyroxene completely dissolves in garnet at 620 km depth.

Irifune *et al.*'s (1986) experiments on a piclogitic composition lead to the conclusion that not only the Ca-poor pyroxene but also clinopyroxene dissolves completely into the garnet phase at 400 km depth. This gives a pyroxene-free garnetite composition at the 400 km discontinuity, and hence a too-large jump in velocity and density for Anderson & Bass's eclogitic and piclogitic compositions.

Transition region 400–650 km

Anderson & Bass (1986) assume that this region is dominated by a clinopyroxene–garnet composition. At 550 km depth, 60 per cent of the clinopyroxene is dissolved in the garnet phase as majorite and coexists with spinel and orthopyroxene-majorite. At the bottom of the transition layer all pyroxene is present as majorite. They argue that only this composition, with clinopyroxene gradually changing to majorite, can explain the low velocities and high gradients in the transition region. Weidner (1985, 1986) demonstrates that his pyrolite model does account for the observed high gradient and concludes that the pyroxene to garnet and excess Ca-poor-pyroxene to spinel plus stishovite transformations give the main contributions. The last transformation should account for the possible 550 km jump in velocity. The main difference between Weidner's and Anderson & Bass's models is the yet unmeasured shear modulus of majorite, and whether orthopyroxene is present down to 500 km depth. The importance of the value of the bulk modulus of majorite and its pressure derivative is demonstrated by Akaogi *et al.* (1987). Their estimate disagrees with previous results by Jeanloz (1981) and reduces the bulk sound velocity in the transition zone, making a pyrolite mantle composition an acceptable model. Bass & Anderson's (1984) calculations were based on high bulk modulus values for majorite.

Recent measurements on natural peridotite by Takahashi & Ito (1987) showed an absence of orthopyroxenes above 13 GPa, or 400 km depth. As noted before, Irifune *et al.* (1986) demonstrate that in a piclogite model nearly all pyroxene is transformed completely to pyroxene-free garnetite in the transition zone, thus removing a key argument for a piclogitic mantle. Laboratory measurements at pressures up to 24 GPa and temperatures up to 2400 °C (Sawamoto 1986) show that the phase boundaries between modified spinel and spinel remain linear, but that the above mentioned interpretation of the 550 km discontinuity has to be rejected. He also proposes a phase transition of pyroxene to a garnet-like structure. Takahashi & Ito (1987) find that the modified spinel to spinel transition does coincide with the 550 km discontinuity. Although more experimental work is required, they also find some evidence for a diopside-pyroxene to 'Ca-P' transition at 550 km depth.

Models involving mechanical properties

The models described in the last section are based on an average Earth structure without lateral variations. In this chapter we will discuss two models that account for differences between geological provinces.

Tectosphere model

Jordan (1975, 1978, 1981) investigated the contrast in upper mantle properties between old continents and old oceans. Application of the thermal-boundary layer model (as developed in plate tectonic theory) to continents preclude the existence of differences in chemical, mechanical or thermal properties beneath 100–150 km depth. However, observations of ScS and multiple ScS traveltimes (Sipkin & Jordan, 1975, 1976, 1980) were interpreted as showing velocity contrasts to greater depth. In the tectosphere model, this difference is treated by invoking a thick 'root' or chemical boundary layer, consisting mainly of peridotite, depleted in basaltic components. Following 10–20 per cent partial melting, the melt phase migrates upward and the root becomes less dense. This effect not only compensates for the temperature, but stabilizes a more than 200 km thick thermal boundary layer against convective disruptions. Anderson (1979b) has argued against this hypothesis, because of a lack of convincing seismological evidence that continents and oceans differ in structure beneath 200 km depth.

Lithospheric doubling

Lithospheric doubling is defined by Vlaar (1982, 1983) as horizontal subduction of young (<30 Ma) oceanic lithosphere, obducted by a continental or oceanic lithosphere. It is proposed to be a general phenomenon in recent plate tectonics and provides a successful scenario for the Alpine orogeny (Vlaar & Cloetingh 1984). Lithospheric doubling implies a strongly stratified upper mantle to a few hundreds of km depth. Density should increase in the top of the lithospere, but may be followed by a density drop where the second harzburgite layer is present. This is an unstable situation, but may 'freeze' in (Nolet *et al.* 1986b).

Hypothesis testing

Both the tectosphere and lithospheric doubling concept can be used for interpretation of the portion of our models shallower than 400 km. To examine the tectosphere concept, we seek the depth below which there are no differences in mantle structure between geological provinces, in our case the Baltic shield (SCSH2) and west-European platform (WEPL2). Lithospheric doubling implies a strongly layered upper mantle and specifically an eclogitic layer that might

mark the top of an obducted young ocean. The two models are mutually exclusive.

Petrological interpretation

The assumptions in the hypothesis testing of the pyrolite and piclogite model, that acoustic velocities can be projected to greater depths along adiabats, is not valid for the upper 200–400 km. Nolet *et al.* (1986b) therefore parametrized a geotherm for this region and used laboratory measurements of seismic velocities at room temperature and pressure and their isothermal and isobaric derivatives with respect to pressure and temperature. Using the assumed geotherm, they constructed velocity curves for the most important mantle minerals. Although the laboratory measurements of the derivatives with respect to pressure and density are not very accurate, an important conclusion was reached: temperature and pressure effects cannot themselves cause high gradients in v_S and ρ. As a consequence, large velocity or density gradients must be interpreted in terms of a change in mineralogy, chemical composition or partial melting.

Comparison between the present and preliminary model shows that the shear velocity contrast between the high-velocity lid and the low-velocity zone is greater in WEPL2 than in WEPL1. The high-velocity lid in WEPL2 is confined to 80–140 km depth. The corresponding density gradient increases in both models. The average density in the 80–140 km depth interval amounts to 3.45 g cm^{-3} and requires the presence of garnet, since olivine, orthopyroxene and clinopyroxene give densities of approximately 3.3 g cm^{-3} at these depths (Nolet *et al.* 1986b). Thus the interpretation of this high-velocity/high-density region as an eclogitic layer (Nolet 1977) remains the most plausible, although care should be taken in the extrapolation of laboratory measurements when dealing with complex phase diagrams (Wood 1987). No density inversion, as observed by Nolet (1977), is resolved at greater depth.

The eclogitic layer near 100 km depth can be explained by the lithospheric doubling concept, since the basalt of the obducted ocean lithosphere is transformed to eclogite. A density inversion marking the underlying harzburgite layer may not be resolved.

Since the velocities in the low-velocity zone do not correspond to any obvious mineralogy, partial melting is assumed. Since a possible Lehmann discontinuity is not resolved, the gradient between 200 and 400 km depth is not very well determined. Both models, WEPL1 and WEPL2, exhibit the same gradient from 250 to 350 km depth. The deeper part of the model can be compared with the shear velocity and density predicted for pyrolite and piclogite compositions by Bass & Anderson (BA), (1984) and Weidner (WE), (1985) (Figs 14 and 15). For the shear velocity, the uppermost 350 km is not well fit by either model, in accordance with our previous conclusions. The velocity jump at 400 km depth agrees well with BA-piclogite and WE-pyrolite. A total disagreement exists with BA-pyrolite. The change in gradient between 500 and 600 km depth is compatible with WE-pyrolite only at greater depth. This feature is not well resolved; our inversion does not show the gradient as in the BA- models. Density is not well resolved below 150 km, but we can observe some features. The jump in density at 400 km depth is most likely larger than predicted by the BA-piclogite model. Inversions with a density difference smaller than in WEPL2 generate a sharp density inversion after the 400 km discontinuity, which appears unrealistic. At greater depths all models coincide with respect to density.

Finally, we compared our Baltic shield model (SCSH2) with WEPL2 (Fig. 13). A general and well-resolved difference between SCSH2 and WEPL2 is the low-velocity layer at 160–220 km depth. This supports the tectosphere hypothesis of significant differences between shield and platform structures at least to 250 km depth. This is presumably because, since the shield is much cooler, no partial melting occurs. In the upper part of the transition zone, shear velocity seems to be lower under the shield,

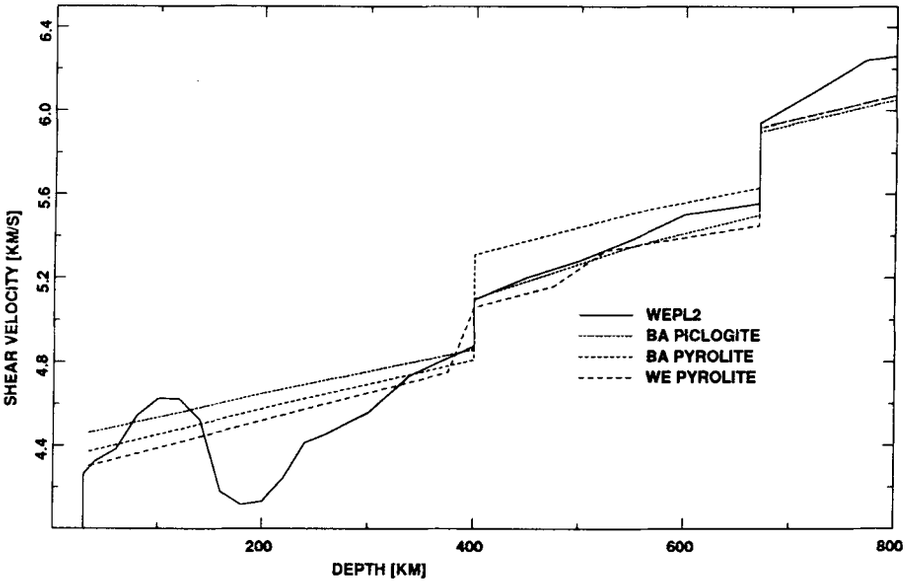

Figure 14. Shear velocity as a function of depth for WEPL2, Bass & Anderson (BA) piclogite and pyrolite, and Weidner (WE) pyrolite.

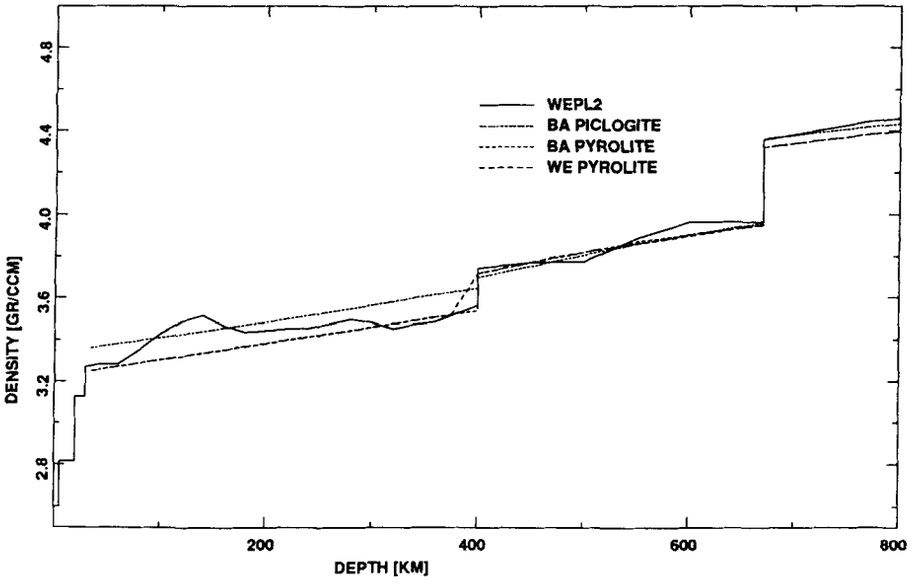

Figure 15. Density as a function of depth for WEPL2, Bass & Anderson (BA) piclogite and pyrolite, and Weidner (WE) pyrolite.

suggesting that there are differences in structure between shield and platform down to 500 km depth. This observation may explain why PREM, an average global model, exhibits systematically lower shear velocity values than our inversion results. A difference in depth of the 400 km discontinuity does not influence the shear velocity gradients in the transition zone, as shown previously. The major difference in density structure is a possible density inversion under the Baltic shield between 200 and 350 km depth.

CONCLUSIONS

Interpretations of shear velocity and density models, obtained by inversion of fundamental and higher mode Rayleigh wave phase velocities, enables us to investigate the structure and composition of the west-European platform. The most remarkable result is the existence of a high-velocity and density layer, interpreted as an eclogite layer, at approximately 100 km depth. It is underlain by a pronounced low-velocity layer, presumably indicating partial melting. The transition zone is characterized by high shear velocities and a change in shear velocity gradient at approximately 600 km depth. An interpretation in terms of a pyrolite or piclogite structure is not possible, because of the uncertainties in elasticity parameters of the high-pressure phases. However, the density jump at the 400 km discontinuity favours a pyrolite composition. The existence of an eclogite layer supports the lithospheric doubling theory.

In the inversion procedure it became apparent that the assumption of discontinuities in the starting model is of crucial importance for the inversion result. Introduction of these discontinuities, however, can lead to non-linear effects and as a result the linearized inversion procedure is no longer valid. Therefore, we will use the models produced in this study in a non-linear inversion procedure and test their validity as average models. Comparison with results from body wave modelling by Paulssen (1987) shows similarities, not only in the upper part of the model, but also in the high shear velocity values in the transition zone.

The model for the Baltic shield is less reliable, because we compare a low-frequency data set for shield plus platform with a high-frequency data set for the platform. As a result we can only look at gross differences. A major feature like the low-velocity zone is clearly not present under the shield structure, while density seems to be lower under the shield from 200 to 350 km depth. In the transition layer there is evidence for a difference in shear velocity between shield and platform, suggesting a difference in structure between shield and platform down to 5 km depth.

ACKNOWLEDGMENTS

I thank Guust Nolet for many stimulating discussions and helpful advice, and Seth Stein for critically reading the manuscript. The Network of Autonomously Recording Stations (NARS) is the Dutch contribution to the European Geotraverse Project (EGT). NARS has been financed by AWON, the Earth Science branch of the Netherlands Organization for the Advancement of Pure Research (ZWO).

REFERENCES

Akaogi, M. & Akimoto, S., 1977. Pyroxene-garnet solid solution equilibria in the system $Mg_4Si_4O_{12}$–$Mg_3Al_2Si_3O_{12}$ and $Fe_4Si_4O_{12}$–$Fe_3Al_2Si_3O_{12}$ at pressures and temperatures, *Phys. Earth planet. Inter.*, **15**, 90–106.

Akaogi, M. & Akimoto, S., 1979. High-pressure phase equilibria in a garnet lherzolite, with special reference to Mg^{2+}–Fe^{2+} partitioning among constituent minerals, *Phys. Earth planet. Inter.*, **19**, 31–51.

Akaogi, M., Navrotski, A., Yagi, T. & Akimoto, S., 1987. Pyroxene-garnet transformation: thermochemistry and elasticity of garnet solid-solutions, and application to a pyrolite mantle, in *High Pressure Research in Mineral Physics*, pp. 251–260 eds Manghnani, M. H. & Syono, Y., American Geophysical Union, Washington, D.C.

Anderson, D. L., 1979a. The upper mantle transition region: eclogite?, *Geophys. Res. Lett.*, **6**, 433–436.

Anderson, D. L., 1979b. The deep structure of continents, *J. geophys. Res.*, **84**, 7555–7560.

Anderson, D. L. & Bass, J. D., 1984. Mineralogy and composition of the upper mantle, *Geophys. Res. Lett.*, **11**, 637–640.

Anderson, D. L. & Bass, J. D., 1986. Transition region of the Earth's upper mantle, *Nature*, **320**, 321–328.

Bass, J. D. & Anderson, D. L., 1984. Composition of the upper mantle: geophysical tests of two petrological models, *Geophys. Res. Lett.*, **11**, 237–240.

Bina, C. R. & Wood, B. J., 1984. The eclogite to garnetite transition—experimental and thermodynamic constraints, *Geophys. Res. Lett.*, **11**, 955–958.

Bina, G. R. & Wood, B. J., 1987. Olivine-Spinel transitions: Experimental and thermodynamic constraints and implications for the nature of the 400-km seismic discontinuity, *J. geophys. Res.*, **92**, 4853–4866.

Byrne, C. L. & Fitzgerald, R. M., 1982. Reconstruction from partial information, with applications to tomography, *SIAM J. appl. Math.*, **42**, 933–940.

Byrne, C. L. & Fitzgerald, R. M., 1984. Spectral estimators that extend the maximum likelihood methods, *SIAM J. appl. Math.*, **44**, 425–442.

Calcagnile, G., 1982. The lithosphere-asthenosphere system in Fennoscandia, *Tectonophysics*, **90**, 19–35.

Cara, M., 1978. Regional variations of higher Rayleigh mode phase velocities, a spatial filtering method, *Geophys. J. R. astr. Soc.*, **54**, 439–460.

Cara, M., Nercessian, A. & Nolet, G., 1980. New inferences from higher mode data in Western Europe and Northern Eurasia, *Geophys. J. R. astr. Soc.*, **61**, 459–478.

Dost, B., 1986. Preliminary results from higher-mode surface-wave measurements in western Europe using the NARS array, *Tectonophysics*, **128**, 289–301.

Dost, B., 1987. The NARS array, a seismic experiment in western Europe, *PhD thesis*, Utrecht University, the Netherlands.

Dziewonski, A. M. & Anderson, D. L., 1981. Preliminary reference Earth model, *Phys. Earth planet. Inter.*, **25**, 297–356.

Grand, S. P. & Helmberger, D. V., 1984. Upper mantle shear structure of North America, *Geophys. J. R. astr. Soc.*, **76**, 399–438.

Irifune, T. & Ringwood, A. E., 1987. Phase transformations in primitive MORB and pyrolite compositions to 25 GPa and some geophysical implications, in *High-Pressure Research in Mineral Physics*, pp. 231–242, eds Manghnani, M. H. & Syono, Y. American Geophysical Union, Washington, D.C.

Irifune, T., Sekine, T., Ringwood, A. E. & Hibberson, W. O., 1986. The eclogite-garnetite transformation at high pressure and some geophysical implications, *Earth planet. Sci. Lett.*, **77**, 245–256.

Jeanloz, R. & Thompson, A. B., 1983. Phase transitions and mantle discontinuities, *Rev. Geophys. Space Phys.*, **21**, 51–74.

Jordan, T. H., 1975. The continental tectosphere, *Rev. Geophys. Space Phys.*, **13**, 1–12.

Jordan, T. H., 1978. Composition and development of the continental tectosphere, *Nature*, **274**, 544–548.

Jordan, T. H., 1981. Continents as a chemical boundary layer, *Phil. Trans. R. Soc. Lond.*, **A301**, 359–373.

Kennett, B. L. N., 1985. On regional S, *Bull. seism. Soc. Am.*, **75**, 1077–1086.

Kennett, B. L. N. & Nolet, G., 1978. Resolution analysis for discrete systems, *Geophys. J. R. astr. Soc.*, **53**, 413–425.

Lees, A. C., Bukowinski, M. S. T. & Jeanloz, R., 1983. Reflection properties of phase transition and compositional change models of the 670 km discontinuity. *J. geophys. Res.*, **88**, 8145–8159.

Lehmann, I., 1961. S and the structure of the upper mantle, *Geophys. J. R. astr. Soc.*, **4**, 124–138.

Lerner-Lam, A. L., 1985. Tradeoff between lid thickness and anisotropy using linearized waveform inversion, (abstract), *EOS, Trans. Am. geophys. Un.*, **66**, 966–967.

Lerner-Lam, A. L. & Jordan, T. H., 1983. Earth structure from fundamental and higher-mode waveform analysis, *Geophys. J. R. astr. Soc.*, **75**, 759–798.

Lerner-Lam, A. L. & Jordan, T. H., 1987. How thick are the continents?, *J. geophys. Res.*, **92**, 14007–14026.

Leven, J. H., 1985. The application of synthetic seismograms to the interpretation of the upper mantle *P*-wave velocity structure in northern Australia, *Phys. Earth planet. Inter.*, **38**, 9–27.

Leveque, J.-J. & Cara, M., 1983. Long-period Love wave overtone data in North America and the Pacific Ocean: new evidence for upper mantle anisotropy, *Phys. Earth planet. Inter.*, **33**, 164–179.

Liu, L., 1980. The mineralogy of an eclogitic earth mantle, *Phys. Earth planet. Inter.*, **23**, 262–267.

Mantovani, E., Schwab, F., Liao, H. & Knopoff, L., 1977. Teleseismic Sn: a guided wave in the mantle, *Geophys. J. R. astr. Soc.*, **51**, 709–726.

Mayer-Rosa, D. & Mueller, St., 1973. The gross velocity–depth distribution of *P* and *S* waves in the upper mantle of Europe from earthquake observations, *Z. Geophys.*, **39**, 395–410.

Michette, A. G., Darling, A. M., Fiddy, M. A., Ward, W. A. & Franklin, E., 1984. Resolution enhancement of well log and seismic data, *Geophys. Prosp.*, **32**, 564–580.

Mitchell, B. J., 1984. On the inversion of Love and Rayleigh-wave dispersion and implications for Earth structure and anisotropy, *Geophys. J. R. astr. Soc.*, **76**, 233–242.

Moore, R. O. & Gurney, J. J., 1985. Pyroxene solid solution in garnets included in diamond, *Nature*, **318**, 553–555.

Nakada, M. & Hashizume, M., 1983. Upper mantle structure beneath the Canadian shield derived from higher modes of surface waves, *J. Phys. Earth*, **31**, 387–405.

Nolet, G., 1975. Higher Rayleigh modes in Western Europe, *Geophys. Res. Lett.*, **2**, 60–62.

Nolet, G., 1976. Higher modes and the determination of upper mantle structure, *PhD thesis*, Utrecht University, the Netherlands.

Nolet, G., 1977. The upper mantle under Western Europe inferred from the dispersion of Rayleigh modes, *Z. Geophys.*, **43**, 265–286.

Nolet, G., 1978. Simultaneous inversion of seismic data, *Geophys. J. R. astr. Soc.*, **55**, 679–691.

Nolet, G. & Panza, G. F., 1976. Array analysis of seismic surface waves, limits and possibilities, *Pure appl. Geophys.*, **114**, 775–790.

Nolet, G. & Vlaar, N. J., 1982. The NARS project, Probing the Earth with a large seismic antenna, *Terra Cognita*, **2**, 17–25.

Nolet, G., Dost, B. & Paulssen, H., 1986a. Intermediate wavelength seismology and the NARS experiment, *Ann. Geophys.*, **4**, 305–314.

Nolet, G., Dost, B. & Paulssen, H., 1986b. The upper mantle under Europe: an interpretation of some preliminary results from the NARS project, *Geol. Mignbouw*, **65**, 155–165.

Nolet, G., van Trier, J. & Huisman, R., 1986. A formalism for nonlinear inversion of seismic surface waves, *Geophys. Res. Lett.*, **13**, 26–29.

Oxburgh, E. R., 1980. Mantle Mineralogy and Dynamics, in *Proceedings of the Enrico Fermi International School of Physics*, Vol LXXVIII, pp. 247–269, eds Dziewonski, A. & Boschi, E., North Holland Publishing Company, Amsterdam.

Panza, G. F., Schwab, F. A. & Knopoff, L., 1973. Multimode surface waves for selected focal mechanisms 1. Dip-slip sources on a vertical fault plane, *Geophys. J. R. astr. Soc.*, **34**, 265–278.

Panza, G. F., Mueller, St. & Calcagnile, G., 1980. The gross features of the lithosphere–asthenosphere system in Europe

from seismic surface waves and body waves, *Pageoph.*, **118,** 1209–1213.

Paulssen, H., 1987. Lateral heterogeneity of Europe's upper mantle by body wave modelling, *Geophys. J. R. astr. Soc.*, **91,** 171–199.

Paulssen, H., 1988. Evidence for a sharp 670-km discontinuity as inferred from *P* to *S* converted waves, *J. geophys. Res.*, **93,** 10489–10500.

Ringwood, A. E., 1975. *Composition and Petrology of the Earth's Mantle,* McGraw–Hill, New York.

Ringwood, A. E., 1979. *Origin of the Earth and Moon,* Springer–Verlag New York.

Ringwood, A. E., 1982. Phase transformations and differentiation in subducted lithosphere: implications for mantle dynamics, basalt petrogenesis and crustal evolution, *J. Geol.*, **90,** 611–643.

Sawamoto, H., 1986. Single crystal growth of the modified spinel (β) and spinel (γ) phases of (Mg, Fe)$_2$SiO$_4$ and some geophysical implications, *Phys. Chem. Minerals,* **13,** 1–10.

Seidl, D., 1971. Spezielle probleme der ausbreitung seismischer oberflachenwellen mit beobachtungsbeispielen aus Europa, *PhD thesis,* University of Karlsruhe, FRG.

Sipkin, S. A. & Jordan, T. H., 1975. Lateral heterogeneity of the upper mantle determined from travel times of ScS, *J. geophys. Res.*, **80,** 1474–1484.

Sipkin, S. A. & Jordan, T. H., 1976. Lateral heterogeneity of the upper mantle determined from the travel times of multiple ScS, *J. geophys. Res.*, **81,** 6307–6320.

Sipkin, S. A. & Jordan, T. H., 1980. Multiple ScS travel times in the western Pacific: Implications for mantle heterogeneity, *J. geophys. Res.*, **85,** 853–861.

Snieder, R., 1987. Surface wave scattering theory, with applications to forward and inverse problems in seismology, *PhD thesis,* Utrecht University, the Netherlands.

Spakman, W., 1986. Subduction beneath Eurasia in connection with the mesozoic Tethys, *Geol. Mijnbouw,* **65,** 145–153.

Takahashi, E. & Ito, E., 1987. Mineralogy of mantle peridotite along a model geotherm up to 700 km depth, in *High Pressure Research in Mineral Physics,* pp. 427–437, eds Manghnani, M. H. & Syono, Y., American Geophysical Union, Washington, D.C.

Vlaar, N. J., 1982. Lithospheric doubling as a cause of intra-continental tectonics, *Proc. R. Neth. Ac. Sci.*, **B85,** 469–483.

Vlaar, N. J., 1983. Thermal anomalies and magmatism due to lithospheric doubling and shifting, *Earth planet. Sci. Lett.*, **65,** 322–330.

Vlaar, N. J. & Cloetingh, S. A. P. L., 1984. Orogeny and ophiolites: plate tectonics revisted with reference to the Alps, *Geol. Mijnbouw,* **63,** 159–164.

Weidner, D. J., 1985. A mineral physics test of a pyrolite mantle, *Geophys. Res. Lett.*, **12,** 417–420.

Weidner, D. J., 1986. Mantle model based on measured physical properties of minerals, in *Advances in Physical Geochemistry,* vol. 6, pp. 251–274, ed. Saxena, S., Springer-Verlag, New York.

Wielandt, E. & Knopoff, L., 1982. Dispersion of very long-period Rayleigh waves along the East-Pacific Rise: Evidence for *S* wave velocity anomalies to 450 km depth, *J. geophys. Res.*, **87,** 8631–8641.

Wiggins, R. A., 1972. The general linear inverse problem: Implication of surface waves and free oscillations for Earth structure, *Rev. Geophys. Space Phys.*, **10,** 251–285.

Wood, B. J., 1987. Thermodynamics of multicomponent systems containing several solid solutions, *Rev. Mineralogy,* **17,** 71–95.